

***INVESTIGATION OF REGIONAL AND SEASONAL VARIATIONS IN MARINE
BOUNDARY LAYER CLOUD PROPERTIES FROM MODIS OBSERVATIONS***

M. P. Jensen*, A. M. Vogelmann, and E. Luke
Brookhaven National Laboratory, Upton, NY

W. D. Collins
National Center for Atmospheric Research, Boulder, CO

G. J. Zhang
Scripps Institution for Oceanography, La Jolla, CA

April 2007

*Submitted to
J. Climate*

Environmental Sciences Department/Atmospheric Sciences Division

Brookhaven National Laboratory

P.O. Box 5000
Upton, NY 11973-5000
www.bnl.gov

* Corresponding author: Dr. Michael P. Jensen, Brookhaven National Laboratory, Atmospheric Sciences Division,
Bldg 490D, Upton, NY 11973-5000; (631) 344-7021; mjensen@bnl.gov.

Notice: This manuscript has been authored by employees of Brookhaven Science Associates, LLC under Contract No. DE-AC02-98CH10886 with the U.S. Department of Energy. The publisher by accepting the manuscript for publication acknowledges that the United States Government retains a non-exclusive, paid-up, irrevocable, world-wide license to publish or reproduce the published form of this manuscript, or allow others to do so, for United States Government purposes.

Abstract

To aid in understanding the role that marine boundary layer (MBL) clouds play in climate and assist in improving their representations in general circulation models (GCMs), we quantify their long-term microphysical and macroscale characteristics using observations from the Moderate Resolution Imaging Spectroradiometer (MODIS) instruments aboard the National Aeronautic and Space Administrations' (NASA's) Terra satellite. We use five years of MODIS pixel-level cloud products from oceanic study regions off the west coasts of California, Peru, Canary Islands, Angola and Australia where these cloud types are common. We characterize their organization (macroscale structure), the associated microphysical properties, and the seasonal dependence of their variations. MBL mesoscale structure is quantified using effective cloud diameter, C_D , which we introduce here as a measure of bulk cloud organization that is straightforward to compute and provides descriptive information beyond that offered by cloud fraction. The interrelationships of these characteristics are explored while considering the influences of the MBL state such as the MBL depth and the occurrence of drizzle.

Several commonalities emerge for the five study regions. MBL clouds contain the best natural examples of plane-parallel clouds, but overcast clouds occur in only about 10% of the scenes, which emphasizes the importance of representing broken MBL cloud fields in climate models. Mesoscale organization (larger C_D) and the frequency of MBL cloud occurrence are related to the seasonal cycle of MBL depth. The monthly cloud occurrence peaks with the deepest boundary layers, when the fractions of scenes characterized as “overcast” and “clumped” increase at the expense of the “scattered” scenes. Cloud liquid-water path and visible optical depth trend strongly with C_D , with the largest values occurring for scenes that are drizzling. However, considerable inter-regional differences exist in these trends, suggesting that different

regressions are needed for each region. For peak versus off-peak months, the fraction of drizzling scenes as a function of C_D are essentially the same for either California, Canary, and only differ slightly for Angola, which suggests that a single probability distribution function for drizzle occurrence might be used per region in climate models. The patterns are quite different for Peru and Australia; so the contrasts among regions may offer a test bed for model simulations of MBL drizzle occurrence. The variability of these MBL cloud properties will have implications to the Earth's radiative energy balance, which will be examined in future work.

1. Introduction

Marine boundary layer (MBL) clouds represent a climatologically significant influence on the global energy and water cycle (Randall et al. 1984). Because they possess an albedo that is much larger than the underlying ocean surface, these clouds cause a significant decrease in the amount of solar radiation absorbed in the ocean's mixed layer, with minimal compensation in thermal radiation emitted to space. In fact, observations of the top-of-atmosphere radiation balance measured by the Earth Radiation Budget Experiment (ERBE) Satellite and the cloud fields observed by the International Satellite Cloud Climatology Project (ISCCP) show that low clouds provide the largest net radiative cloud forcing of any cloud type (Hartmann et al. 1992). Despite their importance, the albedo of subtropical MBL clouds is poorly simulated by climate models (Zhang et al. 2005; Bender et al. 2006). It has even been shown that their simulation and response to changing environmental conditions is the main source of uncertainty in tropical cloud feedbacks simulated by climate models (Bony and Dufresne 2005). These radiative impacts are influenced by macro- and micro-physical properties of the clouds that are not fully understood, and their accurate representation in climate models is essential for obtaining realistic simulations.

The nature of this problem is shown in Fig. 1, which illustrates the complex structure that often exists within MBL cloud regions. General circulation models (GCMs) that are used for long-term climate simulations typically have a horizontal grid resolution of approximately 300 km; so dramatic variations in MBL cloud structure are possible even within one model grid cell. Such variations clearly have important impacts on the albedo of the system and understanding them will require a description of how the cloud field is organized (on the

macroscale), the associated microphysical properties (e.g., liquid-water path and drop size), as well as their dependence on the atmospheric physical, dynamic and thermodynamic properties.

For some time, satellite-borne instrumentation has provided the means for observing the intricate structure of MBL cloud fields (e.g., Agee 1984). The description of these fields continue to improve with the deployment of more advanced sensors (e.g., Garay et al. 2004), as well as through the considerable advances in retrieving cloud properties from the measured radiances (e.g., liquid-water path and cloud drop size). However, despite these advances, the cloud properties normally available to the broader climate modeling community involve bulk properties such as cloud fraction, which is certainly not sufficient to quantify this structure. A notable exception is the recent work by Wood and Hartmann (2006), who developed a neural net to use pixel-level satellite data to classify the MBL mesoscale cellular convection (MCC) within scenes (e.g., no MCC, closed MCC, open MCC, cellular but disorganized). Their study was performed for two months of data for regions off the coasts of California and Peru.

As such additional cloud structure information becomes available, its utility to the modeling community depends on it being represented (packaged) in variables that can be related to those used in the climate models. The cloud property variations seen in Fig. 1 occur at a scale that is much finer than the model resolution; however, the figure also shows that similar fine scale variations occur across regions that are much larger than the individual variations. This larger scale pattern suggests that they are governed by processes that operate over an area that is much larger than the variations themselves (albeit still smaller than the model resolution, but not minutely so). These features suggest that the governing processes may interact with the mesoscale through mechanisms that could be represented even at the relatively low resolution of most current climate models.

The physical processes that are responsible for structures seen in the MBL cloud fields are not fully understood, but recent research has indicated that the occurrence of drizzle may play a key role in forming and sustaining the observed structures. Observational studies have investigated pockets of open cells (or POCs) that are embedded in otherwise uniform stratocumulus, and resemble broader regions of open mesoscale cellular convection typically found further offshore (Stevens et al. 2005). POCs and open mesoscale cellular convection are long-lived and contain pronounced amounts of drizzle, which is in contrast to the substantially smaller amount of drizzle found in the surrounding unbroken, stratiform MBL clouds. Large eddy simulation–based (LES) studies support that when drizzle processes are included, mesoscale organization emerges in the form of cloud bands, as the well-mixed MBL (with stratiform cloud) transitions into a convective boundary layer regime (Mechem and Kogan 2003). In addition to the greater amounts of drizzle and mesoscale variability, the POCs also differ microphysically from the stratiform MBL cloud regions by having a greater amount of liquid water and larger effective radii (vanZanten and Stevens 2005). Evidence suggests that the differences in precipitation amounts between the POCs and stratiform regions may be caused by different amounts of cloud condensation nuclei available from aerosols (Sharon et al. 2006; Petters et al. 2006; Rosenfeld et al. 2006) although aerosol variations alone may not be sufficient to explain the observed cloud variations (Matsui et al. 2006).

In this paper, to aid in understanding the role MBL clouds play in climate and assist in improving their representations in climate models, we use satellite data to characterize the organization of MBL cloud systems across the globe (macroscale structure), their associated microphysical properties (e.g., liquid-water path and particle size), and the seasonal dependence of their variations. The interrelationships of these characteristics are explored while considering

the influences of the MBL state that include the MBL depth and the occurrence of drizzle. While many prior studies have investigated MBL cloud properties for a specific region or a limited period, additional insights can be obtained by examining global and seasonal (long-term) differences, as has been done by studies that used ship-based observations (e.g., Klein and Hartmann 1993; Norris and Leovy 1994) or satellite data (Rozendaal and Rossow 2003). Our analyses use five full years of satellite data from the Moderate Resolution Imaging Spectroradiometer (MODIS) aboard the National Aeronautic and Space Administrations' (NASA's) Terra satellite to examine the seasonal, inter-regional differences in MBL cloud properties in five oceanic regions where these cloud types are typical. Similar to other work (e.g., Xu et al. 2005, Zhou et al. 2006), we construct probability distribution functions (PDFs) of many of the properties as a means to quantify the property variation across the region. As will be seen, we use extensive amounts of pixel-level satellite data to enable screening and analyses that would not be possible with coarser (gridded) data sets, such as quantifying the cloud-to-cloud scale (macroscale) structure within each MBL scene. The intended use of these relationships is to aid improving GCM representations of MBL clouds, through simulation evaluation and parameterization development of these MBL cloud characteristics.

The study is presented as follows. Section 2 describes the pixel-scale MODIS cloud property retrievals used, including considerations and minor modifications applied to their values. Section 3 describes the methodology that includes the location of the MBL study regions used, and the procedures used to select and screen for MBL scenes of the area of a GCM-grid box (300 x 300 km). Special attention is given to steps taken to minimize the potential uncertainty in the cloud microphysical retrievals that can be caused by partially filled cloud pixels or 3-D effects. This section also describes the calculation of effective cloud diameter,

which we use to quantify the bulk cloud-to-cloud scale structure within each scene. The measure it provides of the cloud macroscale structure is coarse; however, it is simple to compute and provides cloud structure information beyond that available from cloud fraction, yet can be approximated by grid-scale variables computed in GCMs. Section 3 contains the results of the analysis that use five full years of satellite data for multiple MBL cloud regions, which includes differences in the regional and seasonal variations of cloud diameter and their relationship to the depth of the marine boundary layer. We explain how drizzle occurrence is determined from the data, and show how its regional and seasonal variations are related to those in cloud diameter and the cloud microphysical properties (e.g., liquid-water path, drop size, and optical depth). The objective of this study is to determine the seasonal and regional variations that exist in cloud macroscale structure (cloud diameter), drizzle frequency, and their associated microphysical properties, such that they may be used in GCM climate model validation and parameterization development. It is beyond the scope of this study to determine how these interrelationships impact the radiative budget or are affected by factors such as the meteorological state and aerosol properties, which will be the subject of later research.

2. *Terra* MODIS Data

The data used are from the MODIS instrument deployed on NASA's *Terra* satellite that was launched 18 December 1999. *Terra* is a sun-synchronous, polar-orbiting satellite that has an equatorial overpass at approximately the same local time (LT) once daily in the ascending node (22:30 LT) and on the descending node (10:30 LT). The orbit precesses to provide a view of the entire Earth's surface every 1 to 2 days. We only use data from the 10:30 LT overpass because many of the MODIS retrievals we use require solar illumination. The *Terra* MODIS data

collection began in February 2000. Each scan consists of a 2,330 km swath of upwelling radiance measurements in 36 spectral bands from 0.4 to 14.4 μm that have horizontal resolutions ranging from 250 to 1,000 m. The MODIS Atmosphere Team uses combinations of these spectral observations to determine a cloud mask and retrieve cloud physical and radiative properties (Platnick et al. 2003; King et al. 2003). We use Version 4 of the MODIS instantaneous pixel-level cloud product retrievals (MOD06_L2). (With the analysis methodology we employed [described next section], negligible differences were found in most of our MBL cloud statistics when results using Version 4 MODIS cloud products were compared with those using Version 5. The single exception is for effective cloud diameter, which is easily understood and discussed later in the relevant section.)

The MODIS products used here include the cloud mask, the mid-visible cloud optical thickness (τ_{vis} , at 0.66 μm), liquid-water path (LWP), hydrometeor effective radius (R_{eff}), and cloud-top pressure (CTP). These data are provided at a nadir resolution of 1 km, except for the CTP that is 5 km. To place the retrievals in a common framework, the 5-km retrievals are interpolated to the 1-km grid. The MODIS Team derives τ_{vis} and R_{eff} using radiances from three water-absorbing bands (1.6, 2.1, 3.7 μm) and one of three non-absorbing bands (0.65, 0.86, 1.2 μm) based on a library of results for plane-parallel homogeneous liquid and ice clouds (Platnick et al. 2003). The LWP is derived from these quantities using the relation $\text{LWP} = 2/3 \rho \tau_{\text{vis}} R_{\text{eff}}$ (King et al. 1998), where ρ is the density of water. (The MODIS-v4 processing inadvertently used 3/4 instead of 2/3, which we corrected as per the “Known Problems” documentation at http://modis-atmos.gsfc.nasa.gov/MOD06_L2/qa.html.) The MODIS CTPs for clouds below 700 hPa are determined by comparing the 11- μm infrared window brightness temperature with a temperature profile from the National Center of Environmental Prediction (NCEP) analyses

(Menzel et al. 2002). We modified the cloud mask to classify pixels with $LWP < 3 \text{ g m}^{-2}$ as invalid data, since visual inspection suggested that those retrievals were suspect.

Deriving LWP from the cloud optical depth and R_{eff} depends on assumptions about the cloud vertical structure. The equation above makes the common assumption that the liquid-water content (LWC) and R_{eff} are constant with height. However, R_{eff} is representative only of the cloud-top and a proper retrieval of LWP would require the in-cloud profile of R_{eff} (e.g., Chang and Li 2003). Wood and Hartmann (2006) note that observations of MBL clouds indicate that LWC often increases linearly with height from cloud base while cloud droplet concentrations remain approximately constant. They conclude that a more appropriate equation for boundary layer clouds is $LWP = 5/9 \rho \tau_{\text{vis}} R_{\text{eff}}$, which results in LWPs that are 0.83x those that assume constant LWC and R_{eff} with height. This approach is valid for MBL clouds, although observations indicate that it would not be valid for continental boundary layer clouds (Miles et al. 2000). Since this paper deals only with marine boundary layer clouds, we adopt and apply the 0.83 factor to the (corrected) MODIS LWP.

3. Methods and Analysis

a. Marine Boundary Layer Study Regions

We focus our attention on five major subtropical MBL cloud study regions. The general regions are the same as those identified in Loeb and Coakley (1998), but whose areas were expanded based on the ship-observer climatologies shown in Klein and Hartmann (1993) and Norris and Leovy (1994). The additional area allows for capturing the MBL cloud decks within our MODIS study regions, since their locations during the MODIS observation period might

fluctuate relative to their climatology. The five study regions and their latitude and longitudes are given in Table 1 and displayed in Fig. 2. Cloud data over any land surface areas that might intersect the regions are removed from the analysis.

Our objective is to analyze the MBL cloud properties for these five regions throughout multiple seasonal cycles of MODIS observations to enable analyzing cloud occurrence and variations in their microphysical and macrophysical properties. To do so, we acquired five years of the pixel-level *Terra*-MODIS cloud products (MOD06_L2) for our regions from March 2000 to February 2005 from the Goddard Distributed Active Archive Center (DAAC). The data are obtained from the DAAC in the form of granules (the approximate size of a granule is 2030 km x 1354 km), and the part of the granule that was within one of our study regions (Fig. 2) was subsetting and stored for later analysis. Overall, this process involved acquiring 3.9 Terabytes of MOD06_L2 data from the DAAC.

b. Scene Selection

Our goal is to investigate the mean properties of MBL clouds and their associated variability on the scale of a GCM grid box. The size of the grid box used here is 300 km on a side, which is the size typically used by GCMs for long-term climate simulations. One of the reasons for working with the volume-intensive pixel-level MODIS products, rather than the less-voluminous gridded data (e.g., level-3 data), is to enable careful selection and quality control of our MBL scenes. Each data file acquired from the DAAC potentially contains multiple candidate MBL scenes (*i.e.*, one scene per grid box), which are located and evaluated (quality controlled) using an automated set of procedures. A candidate scene is located within a file by moving a 300 km x 300 km window across the region in a stepwise search pattern. If a candidate

scene satisfies the criteria for a MBL scene, its pixels are removed from the search array to prevent being reused in later scenes, thereby ensuring that each scene is independent.

A candidate scene is first screened using MODIS quality control flags and solar geometry requirements. Any portion of the file that contains sunglint is excluded, because it may render cloud retrievals in that region suspect. In some cases, this can exclude half of the data within the file. This has a benefit of also removing data from the forward-scattering direction that can have biases in cloud optical depth retrievals due to variations in cloud-top topography (Loeb and Coakley 1998). To avoid retrieval problems associated with low sun angles (Loeb and Davies, 1996), the solar zenith angle and satellite viewing angles are required to be less than 60° . A minimum cloud fraction of 20% is required, and 90% of a scene's cloud pixels must be valid (i.e., not invalid by the MODIS quality control flags).

Scenes containing significant amounts of other cloud types are rejected. For example, regions containing cirrus cloud fractions greater than 10% are rejected, because it is uncertain that thin cirrus overlying MBL clouds can be detected reliably. To determine whether MBL clouds are the dominant cloud type within a scene, each scene is tested for the presence of low cloud decks with uniform cloud-top heights. This is determined by requiring that the median CTP of the pixels is greater than 650 hPa, and that 50% of the CTPs are within ± 10 hPa of the median. This removes scenes that may contain frontal cloud systems or a significant number of penetrating convective clouds. We note that a CTP of 650 hPa is higher in the atmosphere than expected for MBL clouds; however, this is only used as an upper limit for candidacy and (as will be seen) those that are selected are much lower in the atmosphere, more consistent with typical MBL cloud heights. When a scene is accepted, any remaining pixels that have pressures less than 650 hPa are flagged as invalid for our analysis. This way, if we have a scene dominated by

MBL clouds, but including one penetrating convective cell ($<10\%$ of the cloud pixels), the statistics for the MBL portion can still be used. A final criterion requires that the cloud effective size be relatively constant across the scene, and is described in Section e.

c. Seasonal and Diurnal Aspects of MBL Scene Occurrence

Based on these selection criteria, a total of 39,897 independent MBL cloud scenes are identified within our 5-year data set. The total number of scenes per region is given in Table 1, and the annual cycles of the number of scenes per region are plotted in Fig. 3a. A clear seasonal cycle is found per region, which may be considered as a rough proxy for MBL cloud occurrence. The number of monthly scenes per region can differ from each another by a factor of three or more (Fig. 3a). This can be explained by the different sizes in the study regions (see Table 1), and by the variable fraction of a region's "true" MBL frequency accepted by our analysis after rejecting scenes that are contaminated by high clouds or other quality control issues. The fraction of "true" MBL scenes rejected by such issues will vary between regions and even within a region over its seasonal cycle. Our satellite sampling will be biased towards cases dominated by high-pressure systems, since our method rejects scenes containing a significant number of high-level clouds (10% of cloudy pixels). During peak months, large-scale subsidence generally exists within our regions, which diminishes the chance of high-level clouds; however, this is not the same case during off-peak months, which increases the chances scene rejection. Because of seasonal differences in high cloud occurrence, the seasonal patterns shown in Fig. 3a may be thought of as being representative of the MBL cloud frequency, but they cannot be translated directly into absolute seasonal cycles in MBL cloud occurrence.

Nevertheless, the seasonal cycle found generally agrees well with that observed by Klein and Hartmann (1993), who used 30 years of ship-based observer reports (Woodruff et al. 1987) to define climatologies for similar regions. The months of peak MBL cloud frequency are easily identified and are listed in Table 1, and only minor amounts of interannual variability exist within our seasonal cycles (not shown). We find similar peak months as Klein and Hartmann (1993) for three of the five regions (Canary, Angola, Australia); however, the peaks are slightly shifted for California (theirs are June-August and ours July-September) and Peru (theirs are September-November and ours July-September). These differences could be caused by several obvious differences in the observation methods: the locations of the study regions are slightly different (their regions are subsets of our larger regions); unlike the ship-based observations, our satellite algorithm rejects scenes that are contaminated by high-level clouds or sunglint; there are possible differences caused by the diurnal sampling between the ship-based observations and the *Terra* satellite mid-morning observation time, and our five year study period is not equivalent to the 30 year period they used for their climatology. Also included in Fig. 3 are the geographical distributions of the MBL cloud occurrence within each region, which show that the maxima are generally captured well within our study regions. These distributions have combined all years into a single image, but the general location of the maxima do not shift significantly during the seasonal cycle (not shown) although, of course, their absolute magnitudes are modulated by the seasonal cycle in the total number of scenes given in Fig. 3a.

Klein and Hartmann (1993) concluded from their analysis that the annual cycle of MBL cloud occurrence is closely tied to the annual cycle of static stability in the lower atmosphere. MBL clouds are also influenced by the diurnal cycle of factors such as boundary layer mixing and cloud-top entrainment, which are driven by the differential solar heating and infrared cooling

at cloud top. Generally speaking (e.g., summarized in Comstock et al. 2005), at nighttime infrared cooling causes air parcels to sink and tend to mix (couple) the MBL, as well as entrain drier air aloft at cloud top. As daytime progresses, solar radiation heats the cloud top and reduces the effects of infrared cooling. This reduces the amount of mixing within the MBL and, in particular, below cloud base. This solar heating, assisted possibly by drizzle in the early morning, can ultimately lead to decoupling of the MBL, whereby the mixing no longer extends through the depth of the MBL (i.e., across the cloud and surface-air layers). At nighttime, the infrared cooling reenergizes the MBL mixing (coupling). While this is a broad conceptual view of the diurnal cycle, it is useful to bear in mind that the results presented using data from the *Terra* satellite will tend to capture the mid-morning state of this diurnal cycle, which is generally a transition period between the coupled and decoupled states.

d. Acquiring Scene Statistics & Uncertainties

For each scene that passes this rigorous screening, we compute its cloud fraction and the mean of the cloud pixels for τ_{vis} , LWP and R_{eff} . In addition to the items discussed earlier, these cloud property retrievals can be effected by uncertainties caused by some other considerations that are addressed here. For example, retrievals of cloud properties from satellite data often assume that the cloud within each pixel is overcast, as is assumed for the MODIS retrievals. However, some pixels might only be partially cloud-covered and, if so, they would masquerade to a retrieval algorithm as a thinner cloud (e.g., Oreopolous and Davies 1998). This would lead to overestimations in cloud amounts and R_{eff} , while underestimating visible optical depths, cloud-top altitude, and cloud LWP (Coakley et al. 2005). To minimize the potential impact of this uncertainty, we use a binary cloud mask to locate pixels that reside at the edge of the cloud,

and remove them from our calculations of the mean. From the edge, we remove only one pixel deep into the cloud. We acknowledge that all of these pixels might not be partially cloud-filled and that we might be excluding legitimate cloud variability that exists at cloud edge. However, at least part of this variability will be captured by the neighboring cloud pixels that are not removed, while erroneous retrievals of potentially partially filled pixels would introduce biases with little-to-no compensation. For the calculation of cloud fraction, we have no choice but to use the MODIS cloud mask as is (i.e., include potential partially filled pixels) since their exclusion would only guarantee an underestimation of cloud fraction.

The MODIS cloud retrieval algorithm also makes the common assumption that the radiance field emerging from the cloud can be accurately interpreted using plane-parallel radiative transfer theory. This assumes that 3-D radiative transfer effects are negligible, whether they are pixel-to-pixel exchanges of photons or shadowing of pixels by uneven cloud-top topography (e.g., Marshak et al. 2006). The presence of such 3-D effects can result in retrieval errors in cloud optical depth (Loeb and Davies 1996; Loeb and Coakely 1998; Várnai and Marshak 2002a; Várnai and Marshak 2002b) as well as R_{eff} (Bréon and Doutriaux-Boucher 2005; Cornet et al. 2005; Marshak et al. 2006). Correcting these potential 3-D effects for all our study regions is beyond the scope of this study. However, we note that the following considerations will reduce the systematic effect of retrieval artifacts related to 3-D cloud geometry: (1) excluding the pixels at the edge of the cloud, since 3-D effects are arguably largest at a cloud edge; (2) our MBL scene selection required that the cloud tops have little CTP variation, as would be expected if the cloud tops are following the height of the boundary layer inversion; (3) we seek the central tendency (average) for a scene that is 300 km on a side so a certain amount of cancellation of 3-D effects of opposite sign can be expected in the averaging;

and (4) we only use scenes that have a cloud fraction of 20% or more, which would tend to avoid cumulus fields that are particularly problematic (e.g., Marshak et al. 2006). At least one piece of circumstantial evidence suggests that the effects of such 3-D effects are minimized after augmenting the algorithm and quality control practices used in the MODIS products with our analysis procedure. Marshak et al. (2006) show that, because retrievals using plane-parallel theory cannot treat the shadowing of neighboring pixels caused by cloud-top height variations, such cases will retrieve optical depths that are biased low and R_{eff} that are biased high. However, as will be seen later in this paper, we find the opposite pattern (larger optical depths for scenes correlate with larger R_{eff}), which is also in general agreement with related marine boundary layer observations.

e. Effective Cloud Diameter

The eventual goal of this work is to aid GCM cloud parameterization and, to assist in this endeavor, we desire a property that goes beyond determining the fractional cloud coverage of the scene and quantifies the bulk cloud-to-cloud scale structure within each scene. Information on how the cloud elements are organized within the scene may offer useful descriptive information beyond cloud fraction, since their horizontal distribution might result from (or impact) cloud-top entrainment and/or the state of the MBL coupling/decoupling. To quantify how the clouds within a scene are organized or clustered, we compute its effective cloud diameter, C_D . It is proportional to the average diameter of the clouds within the scene and is defined to be,

$$C_D = \frac{4 \sum_i^N A_i}{\sum_i^N P_i}$$

where A_i and P_i are, respectively, the area and perimeter of the N individual clouds within the scene. (A cloud is a contiguous set of cloud-filled pixels that is surrounded by a ring of cloud-free pixels.) The factor of four converts the ratio to a cloud diameter, such that for a scene containing perfectly circular clouds with diameter D , C_D would equal D . Fig. 4 shows an idealized example of C_D and its advantage relative to using cloud fraction. Each scene is comprised of circular clouds whose radii are the same, but which changes among scenes. Even though the cloud fraction is identical for all scenes, C_D varies by a factor of two, from 0.75 to 1.5L. Thus, C_D provides additional information to cloud fraction about how clouds are organized within a scene.

The calculation of C_D is generally insensitive to the size of the scene (or grid). It is completely insensitive to the size of the scene when the individual clouds are small enough to remain within (not cross) the scene perimeter; however, the maximum value for C_D is limited by the size of the scene. This limit applies when a single large cloud fills the scene completely. In our study with 300 km scenes, the values for C_D range from near zero (very scattered clouds) to a maximum of 300 km (a single, solid cloud deck, or “sheet,” without any holes). Examples of different cloud scenes from MODIS observations and how they are quantified via C_D are given in Fig. 5 for MBL clouds off the coast of California. We emphasize that the calculation of C_D depends only on the scene’s binary cloud mask, and not on the LWP variations among the cloudy pixels. This simplicity lends itself to the speed and stability needed for our multi-year, automated analysis and, as will be seen, C_D correlates well with properties currently available from GCMs, such as cloud fraction and LWP .

The calculation of C_D is robust in that it can be easily calculated for any scene with minimal numerical chatter. Excepting the limit when a single cloud approaches filling the entire

scene, tests of C_D find that it is fairly independent of the scene size used. We tested the stability of C_D by starting with 300 x 300 km scenes and “zoomed” in via multiple size steps, recomputing C_D at each step. Regardless of the initial C_D value, it remained roughly constant until the grid approached 100 km. The only exception was if the scene happened to be centered on the edge of a cloud system where, for example, half of the scene is overcast and the other half is clear. However, since the cloud character is not consistent across the scene, it also would not be desirable (representative) input for our analysis. So, as a final scene selection criterion (in addition to those in Section 3.b), we use this “zoom” procedure to remove scenes that contain cloud edges, and require that the C_D value remain constant to within 50% when the scene is zoomed in by 50% (*i.e.*, 300 km to 150 km). Finally, we tested the sensitivity of C_D calculations to using MODIS Version 4 cloud products and Version 5. The C_D frequency distributions shift slightly towards larger values when Version 5 data are used, with the peak moving from approximately 20 km to 40 km. Such a difference would not change the conclusions discussed in this work, and would even have a minor impact on the appearance of the graphs since C_D is plotted on a logarithmic scale.

f. Relation of cloud diameter to cloud fraction and cloud structure

For the use of our analysis for GCM parameterization and validation efforts, C_D does not need to be computed within a GCM. Rather, it is primarily used here as a means to separate the different classes of cloud fields. However, we do find a general relationship between MBL scene cloud fraction (computed in GCMs) and C_D , which may be useful to translate between the two. Fig. 6a shows how C_D increases with cloud fraction, where the points represent binned-medians of all the MBL cloud scenes in our database. In the limit of large cloud fractions, C_D

has a greater range of values and, therefore, provides a more sensitive measure of bulk cloud structure than cloud fraction. A polynomial fit to the median points is shown for reference and the coefficients of the fit provided. The polynomial is only applicable within the bounds of the data used for the fit, $4 \leq C_D \leq 300$ km, where the lower limit (cloud fraction of 0.2) arises from the limit we set for screening and identifying MBL scenes from other types of clouds. The fit is better than ± 0.02 in cloud fraction, and the average of the absolute deviation between all median points and the fit is within 0.0022. The relationship shown between cloud fraction and C_D is very similar to that obtained if the fits are performed individually per region (not shown) instead of being aggregated into a single fit.

We note that other studies have shown the value in using more sophisticated techniques for MBL cloud identification and classification, such as the neural net used by Wood and Hartmann (2006). They use 32 elements describing the *LWP* power spectrum and 40 elements characterizing the *LWP* probability distribution function to classify the mesoscale cellular convection (MCC) in MODIS scenes (no MCC, closed MCC, open MCC, cellular but disorganized). Ranges of our C_D values will not directly correlate with their categories because they use additional information about the *LWP* spatial structure that is not considered in our classification. However, smaller values of C_D will contain open MCC (among other scattered cloud types), and intermediate values will contain closed MCCs. (Later in Section 4a, these categories will be referred to respectively as “scattered” and “clumped.”)

This point is made clearer if, in addition to C_D , we also consider cloud spacing, defined here as the average distance between clouds (*i.e.*, the diameter of the holes). Although we do not explicitly determine cloud spacing in our analyses, it can be estimated from the scene’s cloud fraction, f_c , and C_D after applying a few assumptions. If we assume that all clouds within the

MBL scene have diameter C_D , and that the clouds (and holes between clouds) are uniformly spaced, the average area between clouds, A_s , is,

$$A_s = \pi \left(\frac{C_D}{2} \right)^2 \frac{(1-f_c)}{f_c}$$

If A_s is represented by an area-equivalent circle, then the average spacing diameter, S_D , is,

$$S_D = 2\sqrt{\frac{A_s}{\pi}}$$

Based on these assumptions, Fig. 6b gives the relative frequency distribution of spacing diameter as a function of C_D for the data from Fig. 6a. The contours fan out in the $\pm y$ -directions relative to the median line shown, and two local maxima are found at spacing diameters of about 10 and 20 km. (The spread in the $\pm y$ -direction suggests an explanation for the distance between the median and the $\pm 25\%$ quartiles shown in Fig. 6a.) The 0.50 contour (representing the greatest concentration of points) is bounded by spacing diameters of about 10 to 30 km, while the C_D values that bound the same contour have a larger range, being from about 5 to 50 km. Although approximate, Fig. 6b shows that there tends to be a correlation between spacing diameter and C_D with a smaller variation in the former, which suggests that C_D alone can represent a large degree of the average scene-to-scene variability in cloud structure.

4. Results

The five years of MODIS-*Terra* data from our five MBL study regions are used to investigate the long-term, broad characteristics of MBL clouds and their variability as a function of geography, season, boundary layer characteristics, and drizzle occurrence.

a. Cloud diameter regional and seasonal variation

The mesoscale organization of MBL clouds can be characterized using the effective cloud diameter. The overall relationship between C_D and the mesoscale organization is summarized in Fig. 7, which shows the cumulative frequency distribution of MBL C_D for all regions and all years combined. For ease of discussion, MBL cloud scenes are divided into three descriptive categories: scattered, $C_D \leq 10$ km; clumped, $10 < C_D \leq 80$ km, and overcast, $C_D > 80$ km. The C_D values used to divide the categories are estimated based on the local maxima in spacing diameter (vertical lines in Fig. 6b), which correlate with the relative modes we identify in the frequency histograms of C_D , as well as from visual inspection of plots of the horizontal distributions of the cloud mask within each category. The percentages of MBL scenes per category (scattered, clumped and overcast) are approximately 20, 70, and 10 %. Stratiform MBL clouds are often sought for natural examples of clouds that approach being plane-parallel, but this figure illustrates that this is a relatively uncommon state for MBL clouds and emphasizes the importance of broken (*i.e.*, scattered or clumped) MBL cloud scenes over the major MBL cloud regions of the globe. Such broken regions may be influenced by the occurrence of POCs and the physical processes operating therein.

The five MBL cloud regions explored in this study show two distinct modes of C_D frequency of occurrence. Fig. 8a shows the partitioning of the scattered, clumped and overcast MBL cloud categories for each of the five regions combining all years. MBL cloud scenes observed for the Peru, California and Angola regions are similar in nature, *i.e.*, for all three regions the greatest fraction of clouds are clumped ($\sim 80\%$), and scattered and overcast occur at nearly equal frequencies ($\sim 10\%$). For Australia and Canary, there are greater fractions of scattered clouds at the expense of both overcast and clumped. This is consistent with the observations by Norris (1998) that showed a greater occurrence of broken clouds in these

regions, and with Klein and Hartmann (1993) who show that the Canary and Australia regions have relatively lower amounts of stratus, stratocumulus, and sky-obscuring fog compared to the other regions.

We next investigate the differences in cloud structure with seasonal cycle and its variation among the regions. We determine the fraction of the scenes per month within the three different ranges of C_D , and show the fractions per category as a function of the seasonal cycle (Figs. 8b-f). The California, Peru, and Angola regions are dominated by clumped clouds, and their fraction of overcast clouds increase during the peak months at the expense (reduction) in scattered cloud fraction. The Canary and Australia regions exhibit much larger amplitudes in the seasonal cycle of clumped and scattered cloud with the maximum (minimum) frequencies of clumped (scattered) clouds occurring during the peak months. This has important implications for the parameterization of these cloud types in climate models because these different cloud categories have very different impacts on the energy and water balance of the ocean-atmosphere system and likely are influenced by different dynamical mechanisms.

A more quantitative assessment of the differences in C_D between regions and seasons is shown in Fig. 9, which gives the relative frequency of occurrence of C_D for all regions (Figs. 9a, b). The frequencies are partitioned by the three peak months of MBL cloud occurrence (defined in Table 1) and the nine off-peak months. These plots show two distinct groups of regional characteristics, where California, Peru and Angola form one group and Australia and Canary form the other. The distributions of the California group tend to have larger C_D than the Australia group (during both peak and off peak months), and the Australia group has a much larger fraction of C_D less than 10 km. This is consistent with the greater fraction of scattered clouds in the Australia and Canary regions shown in Fig. 8a. Figs. 9c,d clarify the differences in

the frequency distributions of C_D between peak and off peak months using the California and Australia regions. In both regions there is a clear shift towards larger values of C_D during the peak months (*i.e.*, there is a greater proportion of overcast cloud scenes). Similar plots for Angola, Australia, and Peru (not shown) reveal similar shifts.

b. Relation to MBL depth

In order to relate the seasonal cycle of cloud occurrence and cloud structure with the characteristics of the atmosphere, we consider their relationship with MBL depth. The MOD06_L2 cloud data files provide surface pressure (from the GDAS1 6-hourly global analysis) and an estimate of the cloud-top pressure (based on the NCEP profile and the MODIS observations). We use the difference between the surface and cloud-top pressure as a proxy for the MBL depth (Lilly 1968). Fig. 10 (top) shows the seasonal cycle of the monthly median MBL depth for all regions. We offset the horizontal axis to indicate “month relative to the middle of its peak month” (*i.e.* 0 is the mid-point of the peak months for each region). There is a strong seasonal cycle in MBL depth in the Australia and California regions, with the deepest MBLs occurring one month prior to the peak MBL cloud occurrence. The deepest boundary layers in the Canary region occur just as the peak MBL cloud occurrence is ending, while Peru and Angola show very little variability in the monthly median MBL depths. Another interpretation of the relation between MBL depth and cloud diameter is offered by Fig. 10 (bottom) where the median C_D is presented as a function of MBL depth (in 20 hPa bins). All regions show a similar pattern where the largest C_D corresponds with the deepest MBLs. Scattered cloud conditions tend to occur for the shallower MBL depths while the mesoscale organization or MBL increases with MBL depth. This pattern of increasing mesoscale organization with increasing MBL depth is

consistent with the results of Wood and Hartmann (2006). They found an increase in cloud length-scale as a function of the depth of the MBL for both open and closed cell convection in the California and Peru regions. The importance of MBL depth in determining the mesoscale organization, and consequently the cloud diameter, is thus supported through these figures.

c. Relation to scene drizzle occurrence

Previous studies of MBL cloud systems show that the presence of satellite-observed cloud particle effective radii greater than $15\text{ }\mu\text{m}$ generally indicates the presence of drizzle (Pinsky and Khain 2002; Masunaga et al. 2002; Shao and Liu 2004). Such a threshold cannot treat some of the finer details of drizzle occurrence (such as drizzle rate) and, in certain cases, it might even be unable to detect drizzle that occurs at the base of a thick cloud that has not yet involved (entrained) the higher cloud levels in the precipitation process. Nevertheless, since we lack a comprehensive picture of drizzle occurrence within broader MBL cloud systems, even a crude threshold can provide valuable insights into how common drizzle is within MBL cloud systems, the degree of its seasonal and regional variations, as well as the coincident variation in the other cloud microphysical properties. Thus we adopt this threshold and, in its application, require that the scene-mean R_{eff} be greater than or equal to $15\text{ }\mu\text{m}$ for the *scene* to be identified as drizzling. This is a rather stringent requirement since drizzle-sized droplets must occur over a majority of a GCM-sized grid box and, thus, is only used to identify scenes that have a pronounced drizzle mode. We also tested the sensitivity of our drizzle frequencies to the R_{eff} at cloud edges that, as discussed before, may carry greater uncertainty from edge and 3-D effects. We compared the frequency distributions of scene drizzle occurrence when one ring of cloud edge pixels is removed versus three rings. These distributions (not shown) revealed only very

small differences at the smallest values of C_D , which were sufficiently minor that they could just be an artifact caused by elimination of some small clouds in the three-ring removal. Thus, these results suggest that the edge effects should not adversely affect our scene drizzle determination.

Using this criterion, we determine the fraction of MBL scenes that are drizzling for the different seasons and regions. Fig. 11a shows the fraction of MBL cloud scenes that have a dominant drizzle mode over five years of Terra-MODIS observations, which are shown as a function of month relative to the region's peak month. This indicates that the fraction of MBL scenes that are drizzling are greater during the off-peak months than for the peak months. For the California, Canary and Australia regions, the month of peak drizzle occurrence coincides with the peak fraction of scattered cloud scenes (compare with Fig. 8). The Angola region consistently shows a lower frequency of drizzle than any other region, and its month for peak drizzle does not coincide with the peak occurrence of scattered clouds (in fact, they are separated by three months). The former observation is consistent with the results of Masunaga et al. (2002), who suggest that this may be due to cloud-aerosol interactions. Figs. 11b-f show the regional distribution of drizzling MBL cloud scenes for each region. Overall, the patterns show a tendency for the fraction of drizzling scenes to increase going away from the coast. This pattern and some of the finer details in the regional drizzle occurrence are qualitatively consistent with the results Masunaga et al. (2002) and Kawamoto et al. (2001).

The frequency in drizzle occurrence for some regions shows a clear relation to the monthly median MBL depth (Fig. 12). For the California, Canary and Australia regions, drizzle occurrence and MBL depth are anti-correlated, where the deepest MBL depths have the lowest frequency of drizzle. In contrast, the Peru and Angola regions show very little variability in their

monthly median MBL depth (Fig. 10) and, thus, there is very little relation between drizzle fraction and MBL depth.

To illustrate further the relationship between drizzle occurrence and cloud structure, Fig. 13 shows the frequency of drizzle occurrence as a function of C_D for each region, separated for their peak and off-peak months. All regions show that the greatest drizzle occurrence corresponds with smaller values of C_D (i.e. scattered and clumped clouds). The California and Canary regions show similar patterns between their peak and off peak months, and the frequencies for Angola are only slightly different. Peru has dramatically larger frequencies of drizzle during the peak months (compared to off-peak months), which is exactly opposite the pattern for Australia, which shows substantially lower drizzle frequencies during the peak months. These results indicate that there is unique spatial structure of drizzle properties within each region, and that drizzle occurrence is a maximum for scenes with more scattered clouds (i.e., small cloud diameter).

d. MBL cloud optical and microphysical properties

Fig. 14 shows the variation of τ_{vis} , LWP, and R_{eff} as a function of C_D for all regions divided by drizzling and non-drizzling scenes. These plots show that, despite some inter-regional variations, robust trends exist between the C_D and cloud optical and microphysical properties. The τ_{vis} and LWP trend strongly with C_D for all regions, with the greatest values occurring for the drizzling scenes, particularly for LWP. However, there are considerable inter-regional differences in the trends, indicating that different functionalities exist between the regions. R_{eff} is nearly constant at approximately $12 \mu m$ for non-drizzling clouds while for drizzling clouds there is a decrease in R_{eff} for $C_D > 2$.

Fig. 15 shows the monthly variation in the MBL cloud optical and microphysical properties partitioned by drizzling and non-drizzling scenes. The non-drizzling scenes, except for Australia, tend to have the largest τ_{vis} and largest LWP during the region's monthly peaks. This is in phase with the increased fractional occurrence in overcast and clumped scenes (Fig. 8). The Australia region, instead, has a double maximum (with the largest τ_{vis} and largest LWP occurring two months prior to the peak, and 4 months after the peak). For drizzling scenes, the maximum values of τ_{vis} and LWP occur during the monthly MBL peaks for California, Angola and Australia; however, these maxima do not occur in Peru and Canary until one month after the peak season. The seasonal cycle of monthly mean R_{eff} is generally quite different, with lower values during peak months (for drizzling and non-drizzling scenes), and the largest R_{eff} occurring approximately 3 months after the peak season. This suggests that factors other than the seasonal cycle play a role in determining the R_{eff} and, for example, recent studies have indicated that MBL R_{eff} correlate well with aerosol loading (e.g., Matsui et al. 2006).

5. Summary and Conclusions

To aid in understanding the role that MBL clouds play in climate and assist in improving their representations in climate models, we analyzed five years of pixel-level MODIS-Terra observations for five diverse regions of the globe where these cloud types are common. A feature of this study is that the long-term central tendency and seasonal variations of MBL cloud microphysical properties (e.g., LWP, R_{eff} , optical depth) are investigated using mesoscale structure and drizzle occurrence as organizing principles. We minimize the uncertainty in the cloud microphysical retrievals that can be caused by partially filled cloud pixels or 3-D effects by removing the contribution of pixels from the cloud edge (one pixel deep) from our

microphysical property averages. MBL mesoscale structure is quantified using effective cloud diameter, C_D , which is introduced here as a measure of bulk cloud organization that is easy to compute and provides descriptive information beyond that offered by cloud fraction.

Despite expected differences among the regions, some similar organizing principles are found in their macroscale structure (C_D), drizzle frequency, and associated microphysical properties. The following similarities and differences may be used to target work that diagnoses MBL cloud behavior and their functional dependencies in model simulations.

- 1) In all regions, we find a clear seasonal cycle in the frequency of MBL cloud occurrence that is consistent with previous studies (e.g., Klein and Hartmann 1993). They concluded that this seasonal cycle was related to the boundary layer stability. We also find that the seasonal cycle of MBL cloud occurrence is related to the depth of the MBL (estimated from the difference between the surface pressure and the MBL cloud-top pressure) with the months of peak occurrence generally having boundary layers that are deeper than off-peak months.
- 2) Although stratiform MBL clouds are often sought for natural examples of clouds that approach being plane-parallel, we find overall that this is a relatively uncommon MBL state ($\sim 10\%$), which emphasizes the importance of accurately representing broken (*i.e.*, scattered or clumped) MBL cloud scenes in climate models.
- 3) C_D is related to the seasonal cycle through the depth of the boundary layer, with the greatest mesoscale organization (largest values of C_D) tending to occur during the months of peak cloud occurrence and deepest boundary layers. Among the regions, the C_D frequency distributions of peak and off-peak months cluster into two groups that possess similar characteristics, with Australia and Canary in one group (which favors smaller C_D), and Angola, California, and Peru in the other.

- 4) The seasonal cycle of drizzle occurrence generally shows a minimum in the relative drizzle frequency during the months of peak MBL cloud occurrence with maxima during the off-peak months. This is consistent with the correlation of the largest drizzle frequencies occurring for the smaller values of C_D .
- 5) The patterns of drizzle frequency as a function of C_D show marked differences between the regions between peak and off-peak months. The drizzle frequencies for the two periods remain essentially the same for California and Canary, and only slightly different for Angola. This suggests that a single PDF of drizzle frequency versus C_D might be applied per region in climate models. However, the pattern is quite different between Peru and Australia. The patterns for peak versus off-peak months are strikingly different, and the period with the greatest fraction of drizzle frequencies are reversed (Peru greatest during peak months and Australia during off-peak months). The contrast between these two regions may then serve as an excellent test for model simulations of MBL drizzle occurrence.
- 6) Cloud LWP and visible optical depth trend strongly with C_D , with the greatest values occurring for the drizzling scenes. However, there are considerable inter-regional differences in the trends, indicating that different regressions must be used for each region.
- 7) The long-term cloud microphysical properties are also related to this seasonal cycle, where a region's monthly peak MBL frequency tends to have the largest mean τ_{vis} and LWP. However, the mean R_{eff} does not tend to be in phase with the seasonal cycle of MBL cloud occurrence, suggesting that influences not tied to the seasonal cycle exert a great effect (e.g., systematic fluctuations in the number density of cloud-condensation nuclei).

8) Overall, the Canary and Australia regions generally have similar features that are distinctively different from the other regions. They have a more pronounced seasonal cycle in cloud structure, and a larger frequency of scattered cloud scenes, which have lower τ_{vis} and low LWP. These features are in stark contrast to those from Angola and Peru, which have a greater fraction of clumped and overcast clouds that have a larger mean τ_{vis} and LWP. The California region includes characteristics of each of the other regions.

We note that the *Terra* orbit and types of MODIS data used here enable observing the MBL cloud state at approximately the same mid-morning local time each day (about 10:30 AM). However, given the long-term statistics compiled for multiple locations and seasons, we likely capture MBL states that can occur at any point during the diurnal cycle. Also, the variability of MBL cloud properties are dominated by seasonal to annual timescales, and daily to monthly timescales have smaller (but not negligible) variability (Rozendaal and Rossow 2003). Thus, our temporal sampling can capture the dominant variations in MBL cloud properties, although our sampling will favor any subtleties that occur during the mid-morning hours. We also note that our definition of drizzling MBL cloud scenes is subject to several assumptions about the vertical structure of droplet sizes within a cloud layer and how it is related to the drizzle process. Although aerosol-cloud interactions are known to play an important role in MBL cloud microphysics, we have not yet included aerosol observations in our analysis.

The variability of these MBL cloud micro- and macroscale properties will have important impacts on the transfer of radiation through the atmosphere and its subsequent impact on the Earth's energy balance. Future work will explore the relationships between these MBL cloud

properties, the aerosol properties, the large-scale meteorological state, and the accurate representation of the associated radiative transfer in global climate models.

6. Acknowledgements

This work is supported by GWEC grant NASA NAG511716 and the Department of Energy Atmospheric Radiation Measurement Program. The data used in this study were acquired as part of the NASA's Earth Science Enterprise. The retrieval algorithms were developed by the MODIS Science Teams. The raw data were processed by the MODIS Adaptive Processing System (MODAPS) and Goddard Distributed Active Archive Center (DAAC), and are archived and distributed by the Goddard DAAC.

7. References

- Agee, E.M., 1984: Observations from space and thermal convection: A historical perspective. *Bull. Amer. Meteor. Soc.*, **65**, 938–949.
- Bender F. A.-M., H. Rodhe, R.J. Charlson, A.M.L. Ekman, N. Loeb, 2006: 22 views of the global albedo - comparison between 20 GCMs and two satellites. *Tellus-A*, **58** (3), 320-330, doi:10.1111/j.1600-0870.2006.00181.x
- Bony, S., and J.-L. Dufresne, 2005: Marine boundary layer clouds at the heart of tropical cloud feedback uncertainties in climate models, *Geophys. Res. Lett.*, **32**, L20806, doi:10.1029/2005GL023851.
- Bréon, F. M., and M. Doutriaux-Boucher, 2005: A comparison of cloud droplet radii measured from space, *IEEE Trans. Geosci. Remote Sens.*, **43** (8), 1796–1805.
- Chang, F.-L., and Z. Li, 2003: Retrieving vertical profiles of water-cloud droplet effective radius: Algorithm modification and preliminary application. *J. Geophys. Res.*, **108**(D24), 4763, doi:10.1029/2003JD003906.
- Coakley, J. A., M. A. Friedman and W. R. Tahnk, 2005: Retrieval of cloud properties for partly cloudy imager pixels. *J. Atmos. Oceanic Tech.*, **22** (1), 3-17.
- Comstock, K.K., C.S. Bretherton, and S.E. Yuter, 2005: Mesoscale variability and drizzle in Southeast Pacific stratocumulus. *J Atmos. Sci.*, **62** (10): 3792-3807.
- Cornet, C., J.-C. Buriez, J. Riedi, H. Isaka, and B. Guillemet, 2005: Case study of inhomogeneous cloud parameter retrieval from MODIS data. *Geophys. Res. Lett.*, **32**, L13807, doi:10.1029/2005GL022791.

- Garay M., R. Davies, C. Averill and J. Westphal, 2004: Actinoform clouds: Overlooked examples of cloud self-organization at the mesoscale. *Bull. Amer. Meteorol. Soc.*, **85** (10), 1585–1594.
- Hartmann, D. L., M. E. Ockert-Bell, and M. L. Michelsen, 1992: The effect of cloud type on earth's energy balance: Global analysis. *J. Clim.*, **5**, 1281-1304.
- Kawamoto, K., T. Nakajima, and T. Y. Nakajima, 2001: A global determination of cloud microphysics with AVHRR remote sensing. *J. Clim.*, **14**, 2054-2068.
- King, M. D., W. P. Menzel, Y. J. Kauffman, D. Tanre, B. –C. Gao, S. Platnick, S. A. Ackerman, S. A. L. A., Remer, R. Pincus, and P. A. Hubanks, 2003: Cloud and aerosol and water vapor properties, precipitable water, and profiles of temperature and humidity from MODIS. *IEEE Trans. Geosci. Rem. Sens.*, **41**, 442-458.
- King, M. D., S.-C. Tsay, S. E. Platnick, M. Wang, and K. –N. Liou, 1998: Cloud retrieval algorithms for MODIS: Optical thickness, effective radius and thermodynamic phase. ATDB-MOD-05.
- Klein, S. A. and D. L. Hartmann, 1993: The seasonal cycle of low stratiform clouds. *J. Climate*, **6**, 1587-1606.
- Lilly, D. K., 1968: Models of cloud-topped mixed layers under strong inversions. *Quart. J. Roy. Meteor. Soc.*, **94**, 292-309.
- Loeb, N. G. and J. A. Coakley, Jr., 1998: Inference of marine stratus cloud optical depths from satellite measurements: Does 1D theory apply? *J. Climate*, **11**, 215-233.
- Loeb, N. G., and R. Davies, 1996: Observational evidence of plane parallel model biases: Apparent dependence of cloud optical depth on solar zenith angle. *J. Geophys. Res.*, **101**, 1621–1634.

- Marshak, A., S. Platnick, T. Várnai, G. Wen, and R. F. Cahalan, 2006: Impact of three-dimensional radiative effects on satellite retrievals of cloud droplet sizes. *J. Geophys. Res.*, **111**, D09207, doi:10.1029/2005JD006686.
- Masunaga, H., T. Y. Nakajima, T. Nakajima, M. Kachi, and K. Suzuki, 2002: Physical properties of maritime low clouds as retrieved by combined use of Tropical Rainfall Measuring Mission (TRMM) Microwave Imager and Visible/Infrared Scanner 2. Climatology of warm clouds. *J. Geophys. Res.*, **107**, 10.1029/2001JD001269.
- Matsui, T., H. Masunaga, S. M. Kreidenweis, R. A. Pielke Sr., W.-K. Tao, M. Chin, and Y. J. Kaufman, 2006: Satellite-based assessment of marine low cloud variability associated with aerosol, atmospheric stability, and the diurnal cycle, *J. Geophys. Res.*, **111**, D17204, doi:10.1029/2005JD006097.
- Mechem, D.B., Y.L. Kogan, 2003: Simulating the transition from drizzling marine stratocumulus to boundary layer cumulus with a mesoscale model. *Mon. Weath. Rev.*, **131** (10): 2342-2360.
- Menzel, W. P., B. A. Baum, K. I. Strabala, and R. A. Frey, 2002: Cloud top properties and cloud phase – Algorithm theoretical basis document. ATBD-MOD-04.
- Miles, N.L., J. Verlinde, and E.E. Clothiaux, 2000: Cloud droplet size distributions in low-level stratiform clouds. *J. Atmos. Sci.*, **57** (2), 295-311.
- Norris, J. R., 1998: Low cloud type over the ocean from surface observations. Part II: Geographical and seasonal variations. *J. Climate*, **11**, 383-403.
- Norris, J. R. and C. B. Leovy, 1994: Interannual variability in stratiform cloudiness and sea surface temperature. *J. Climate*, **7**, 1915-1925.
- Oreopoulos, L., and R. Davies, 1998: Plane-parallel albedo biases from satellite observations. Part II: Parameterizations for bias removal. *J. Climate*, **11**, 933-944.

- Petters, M.D., J.R. Snider, B. Stevens, G. Vali, I. Faloona, and L.M. Russell, 2006: Accumulation mode aerosol, pockets of open cells, and particle nucleation in the remote subtropical Pacific marine boundary layer. *J. Geophys. Res.*, 111 (D2), D02206, doi:10.1029/2004JD005694.
- Pinsky, M.B. and A.P. Khain, 2002: Effects of in-cloud nucleation and turbulence on droplet spectrum formation in cumulus clouds. *Quart. J. Roy. Meteor. Soc.*, **128**, 501-534.
- Platnick, S., M. D. King, S. A. Ackerman, W. P. Menzel, B. A. Baum, J. C. Riedi and R. A. Frey, 2003: The MODIS cloud products: Algorithms and examples from Terra. *IEEE Trans. Geosci. Rem. Sens.*, **41**, 459-473.
- Randall, D. A., J. A. Coakley, C. W. Fairall, R. A. Kropfli and D. H. Lenshow, 1984: Outlook for research on subtropical marine stratiform clouds. *Bull. Amer. Meteor. Soc.*, **65**, 1209-1301.
- Rozendaal, M.A., and W.B. Rossow 2003. Characterizing some of the influences of the general circulation on subtropical marine boundary layer clouds. *J. Atmos. Sci.* **60**, 711-728.
- Rosenfeld, D., Y. J. Kaufman, and I. Koren, 2006: Switching cloud cover and dynamical regimes from open to closed Benard cells in response to the suppression of precipitation by aerosols. *Atmos. Chem. Phys.*, 6, 2503–2511.
- Shao, H. and G. Liu, 2004: Detecting drizzle in marine warm clouds using combined visible, infrared and microwave satellite data. *J. Geophys. Res.*, **109**, D07205, doi:10.1029/2003JD004286.
- Sharon, T. M., B. A. Albrecht, H. H. Jonsson, P. Minnis, M. M. Khaiyer, T. M. van Reken, J. Seinfeld, and R. Flagan, 2006: Aerosol and cloud microphysical characteristics of rifts and gradients in maritime stratocumulus clouds. *J. Atmos. Sci.*, **63** (3), 983-997.

- Stevens, B., G. Vali, K. Comstock, R. Wood, M. C. van Zanten, P. H. Austin, C. S. Bretherton, and D. H. Lenschow, 2005: Pockets of open cells (POCs) and drizzle in marine stratocumulus. *Bull. Amer. Meteor. Soc.*, **86**, 51-57.
- vanZanten M.C., and B. Stevens, 2005: Observations of the structure of heavily precipitating marine stratocumulus. *J. Atmos. Sci.*, **62** (12), 4327-4342.
- Várnai, T., and A. Marshak, 2002a: Observations and analysis of three-dimensional radiative effects that influence MODIS cloud optical thickness retrievals. *J. Atmos. Sci.*, **59**, 1607–1618.
- Várnai, T., and A. Marshak, 2002b: Observations of three-dimensional radiative effects that influence satellite retrievals of cloud properties. *Idojaras*, **106**, 265–278.
- Wood, R. and D. L. Hartmann, 2006: Spatial variability of liquid water path in marine low cloud: The importance of mesoscale cellular convection. *J. Clim.*, **19**, 1748-1764.
- Woodruff, S. D., R. J. Slutz, R. L. Jenne, and P. M. Steurer, 1987: A Comprehensive Ocean-Atmosphere Data Set. *Bull. Amer. Meteor. Soc.*, **68**, 1239-1250.
- Xu, K.-M., T. Wong, B. A. Wielicki, L. Parker, and Z. A. Eitzen, 2005: Statistical analyses of satellite cloud object data for large ensemble evaluation of cloud models. Part I: Methodology and preliminary results. *J. Climate*, **18** (13), 2497-2514.
- Zhang, M. H., et al., 2005: Comparing clouds and their seasonal variations in 10 atmospheric general circulation models with satellite measurements, *J. Geophys. Res.*, **110**, D15S02, doi:10.1029/2004JD005021.
- Zhou, M., X. Zeng, M. Brunke, Z. Zhang, and C. Fairall, 2006: An analysis of statistical characteristics of stratus and stratocumulus over eastern Pacific. *Geophys. Res. Lett.*, **33**, L02807, doi:10.1029/2005GL024796.

Captions

Table 1. Marine boundary layer (MBL) study regions. The latitude and longitude boundaries are given for each study region. A MBL scene is defined as a 300 km x 300 km grid box that satisfies the selection criteria given in the text. The three peak months refer to the three contiguous months that contain the maximum number of MBL scenes per region. The locations of the regions are plotted in Figure 2. A total of 35,709 independent MBL cloud scenes are identified in our 5-year data set spanning March 2000 to February 2005.

Figure 1. Marine boundary layer cloud scene. This Terra/MODIS scene illustrates the complex structure that often exists within MBL cloud regions. The region shown is about 750 km on a side and is from off the coast of California on January 2, 2005. The image uses reflected radiances for MODIS Band 3.

Figure 2. Map of marine boundary layer (MBL) cloud study regions. Each box indicates the location of a major MBL cloud region, based on the surface-based climatologies in Klein and Hartmann (1993) and Norris and Leovy (1994). The latitude-longitude bounds for each region are given in Table 1. Five-years of data are obtained for each study region, spanning March 2000 to February 2005. Cloud data over any land areas within the study regions are removed from the analyses.

Figure 3. Occurrence frequencies of MBL cloud scenes. (a) Monthly frequencies per region. The numbers of MBL cloud scenes identified per month are combined from all years. (b – f) Regional variations in MBL cloud scene occurrence. For each region, the number of MBL

scenes for all months are combined and gridded. Results are displayed as a fraction of the respective region's maximum grid value (i.e., the maximum value in each 2-D plot is one). Occurrence frequency per region is binned on a 1° grid.

Figure 4. Idealized illustration of effective cloud diameter, C_D . For each scene composed of circular clouds, the cloud fraction is constant at 0.785, but C_D assumes a different value for each scene: 0.75, 1.0 and 1.5 (in arbitrary length units, L). This shows how C_D provides additional information to cloud fraction about how clouds are organized within a scene.

Figure 5. Marine stratus cloud structure and effective cloud diameter, C_D . The three MODIS scenes illustrate the appearance of the cloud LWP as C_D increases sequentially by a factor of five between each scene. Plotted are the \log_{10} of the LWP, where white is clear sky. For each scene, the effective cloud diameter (C_D), fractional cloud cover (f), mean cloud LWP (L) and standard deviation of the LWP (σ) are: A) $C_D=200$ km, $f=99\%$, $L=81$ g m $^{-2}$, $\sigma=35$ g m $^{-2}$; B) $C_D=40$ km, $f=83\%$, $L=189$ g m $^{-2}$, $\sigma=132$ g m $^{-2}$; C) $C_D=8$ km, $f=51\%$, $L=9.7$ g m $^{-2}$, $\sigma=4.3$ g m $^{-2}$.

Figure 6. (a) MBL Cloud fraction and effective cloud diameter. The cloud fractions for all MBL cloud scenes are binned by $\ln(C_D)$ and the medians per bin are plotted (diamonds). A polynomial is fit to the median points (solid curve) and the coefficients provided. The polynomial is only applicable within the bounds of the data used for fitting, $4 \leq C_D \leq 300$ km. The scatter of the individual points about the median curve is indicated by the $\pm 25\%$ quartile levels per bin (dotted lines). (b) Cloud spacing and effective cloud diameter. The space between clouds is expressed as the diameter of an area-equivalent circle (see text for details). The counts

per grid are normalized by the maximum grid value. Contours are 0.0, 0.05, 0.25, 0.50, and 0.75. Line with diamonds gives the median spacing diameters per $\ln(C_D)$ bin. The vertical dashed lines delineate groupings discussed in the text.

Figure 7. Cumulative frequency of occurrence of MBL effective cloud diameters, C_D . All regions and years combined in the plot. For ease of discussion, cloud scenes are divided into three descriptive categories: scattered, $C_D \leq 10$ km; clumped, $10 < C_D \leq 80$ km; and overcast, $C_D > 80$ km. The percentages of MBL scenes per category (scattered, clumped, and overcast) are approximately 20, 70, and 10%.

Figure 8. General MBL cloud structure per region. (a) All years and months are combined per region to show the total composition of each study region is given as a fraction of the three descriptive cloud categories: scattered (S), clumped (C), and overcast (O). (b-f) Seasonal cycle of MBL cloud structure per study region. The relative frequency of occurrence per month is given for each of the three cloud categories. Grey shading indicates the three months of peak MBL cloud occurrence per region.

Figure 9. Relative frequencies of occurrence of C_D per region. (Left panels) All regions are placed on one plot partitioned by peak (top) and non-peak (bottom) months of MBL cloud occurrence. Semicircle groups Canary and Australia, which have similar distributions compared to the other three regions that share similar features (in vice versa). (Right panels) Results for the California (top) and Australia (bottom) regions, partitioned by the three peak (solid) and nine

non-peak (dashed) months. A shift towards larger cloud diameters occurs during the peak months (including the regions not shown).

Figure 10. Boundary layer depth variation among regions. The legend in the bottom panel applies to all curves shown. (Top) Monthly variation in boundary layer depth per study region. Cloud-top pressure is used as a proxy for MBL depth, and its median value is determined per month per region. The abscissa is the month of year, given per region as an offset relative to the middle of its three peak months (i.e., zero is at the middle). The middle of the peak months per region are (from Table 1): Australia-January, Canary-June, California-August, Peru-August, Angola-October. (Bottom) Cloud-top pressure and C_D occurrence. C_D is binned by cloud-top pressures (20 hPa thick) and the median value per bin is plotted per region. All regions show an increase in median C_D with increasing boundary layer depth. The dynamic range in MBL height is larger in the lower panel than in the upper panel because it is binned by C_D and there is a positive correlation found between C_D and MBL height; conversely in the upper panel, the month-to-month dependence on C_D is weaker so the medians are derived from broad, monthly C_D distributions, which mutes the dynamic range of MBL height.

Figure 11. Geographical distribution of drizzle frequency. Drizzle scenes are defined as those with a mean $R_{\text{eff}} \geq 15 \mu\text{m}$ (Pinsky and Khain 2002; Masunaga et al. 2002; Shoa and Liu 2004). (a) Monthly variation of drizzle frequency. Plotted are the fractions of MBL scenes that meet the drizzle criterion per month. The abscissa is the month of year, given per region as an offset relative to the middle of its three peak months (explained in Figure 10). (b-f) Regional distribution of drizzling MBL cloud scenes. Shown are the fractions of MBL scenes that are

drizzling per grid, where the scenes for all months are combined in a single grid per region. Contours of fractional occurrence are given for 0.15, 0.30, 0.45, and 0.60. Note that the total drizzle occurrence would be determined by weighting these fractions by the total frequency of MBL occurrence per grid. Occurrence frequency per region is binned on a 1° grid.

Figure 12. Boundary layer depth versus drizzle occurrence. The fractions of the total number of scenes per month that are drizzling are given as a function of the monthly median boundary layer depth (as defined in Figure 10a).

Figure 13. Frequency of drizzle occurrence as a function of effective cloud diameter, C_D . The drizzle frequencies are partitioned into two groups: the three months of peak MBL cloud occurrence within each region (red line), and the nine off-peak months (blue dashed line). Drizzle occurrence tends to be largest for the smaller values of C_D , which represent the more scattered cloud scenes. The frequencies for Canary and California show little sensitivity to peak versus off-peak timings, while Peru and Australia show pronounced differences in directions that are opposite from each other.

Figure 14. Dependence of MBL cloud properties on effective cloud diameter, C_D . MBL cloud optical depth, τ_{vis} (top), LWP (middle) and R_{eff} (bottom) are plotted as a function of the natural logarithm of C_D . For each curve, all data per region are separated into drizzling (red) and non-drizzling (blue) categories and binned using intervals that are $0.55C_D$ wide; the median for each bin is plotted.

Figure 15. Monthly variation in MBL cloud properties. For each curve, all data per region are separated into drizzling and non-drizzling categories and their monthly means are plotted. Shown are the monthly means of MBL cloud optical depth, τ_{vis} (top), LWP (middle) and R_{eff} (bottom) for drizzling (right) and non-drizzling (left) scenes. The abscissa is the month of year, given per region as an offset relative to the middle of its three peak months (explained in Figure 10).

Table 1. Marine boundary layer (MBL) study regions. The latitude and longitude boundaries are given for each study region. A MBL scene is defined as a 300 km x 300 km grid box that satisfies the selection criteria given in the text. The three peak months refer to the three contiguous months that contain the maximum number of MBL scenes per region. The locations of the regions are plotted in Figure 2. A total of 35,709 independent MBL cloud scenes are identified in our 5-year data set spanning March 2000 to February 2005.

Region Name	Latitude/Longitude Bounds		Total Number of MBL Scenes	Peak 3 Months
Angola	-25 to 0 °N	-20 to 15 °W	12,104	Sep, Oct, Nov
Australia	-40 to -15 °N	85 to 115 °W	3,556	Dec, Jan, Feb
California	20 to 40 °N	-140 to -115 °W	4,994	Jul, Aug, Sep
Canary	5 to 30 °N	-45 to -10 °W	4,847	May, Jun, Jul
Peru	-35 to 5 °N	-100 to -70 °W	10,708	Jul, Aug, Sep

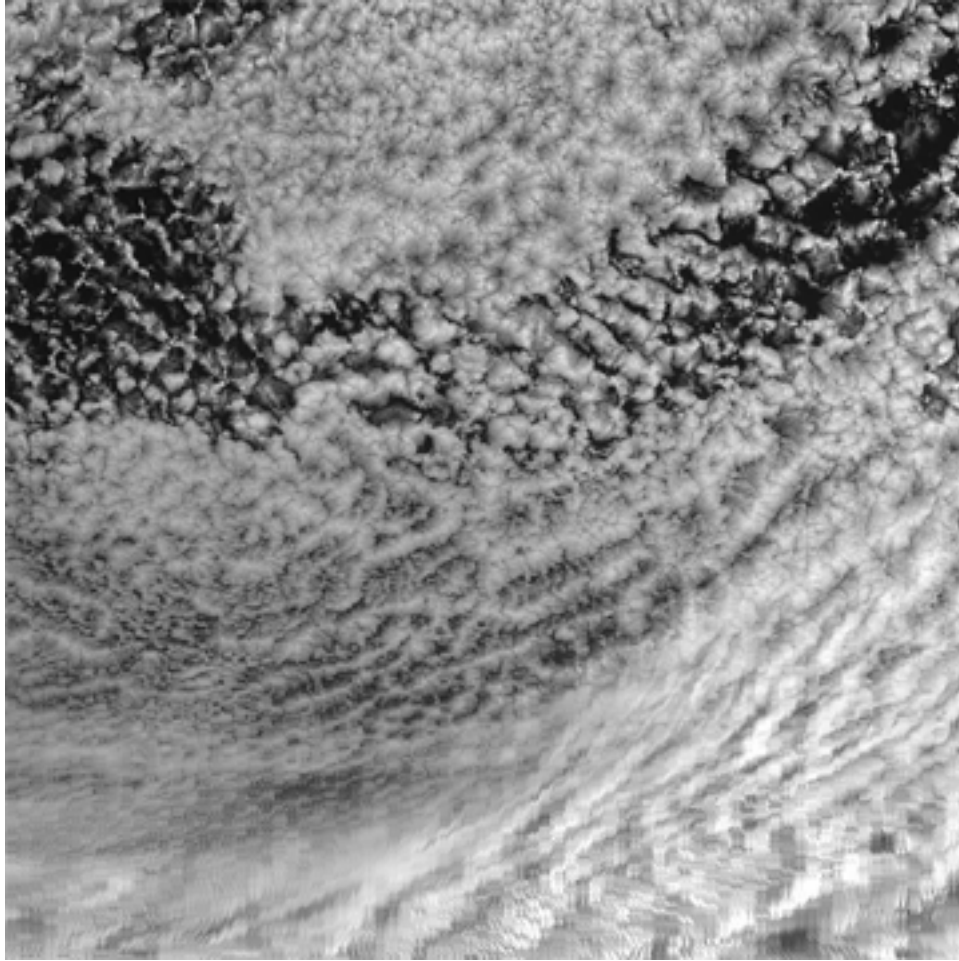


Figure 1. Marine boundary layer cloud scene. This Terra/MODIS scene illustrates the complex structure that often exists within MBL cloud regions. The region shown is about 750 km on a side and is from off the coast of California on January 2, 2005. Marine boundary layer cloud scene. This Terra/MODIS scene illustrates the complex structure that often exists within MBL cloud regions. The region shown is about 750 km on a side and is from off the coast of California on January 2, 2005. The image uses reflected radiances for MODIS Band 3.

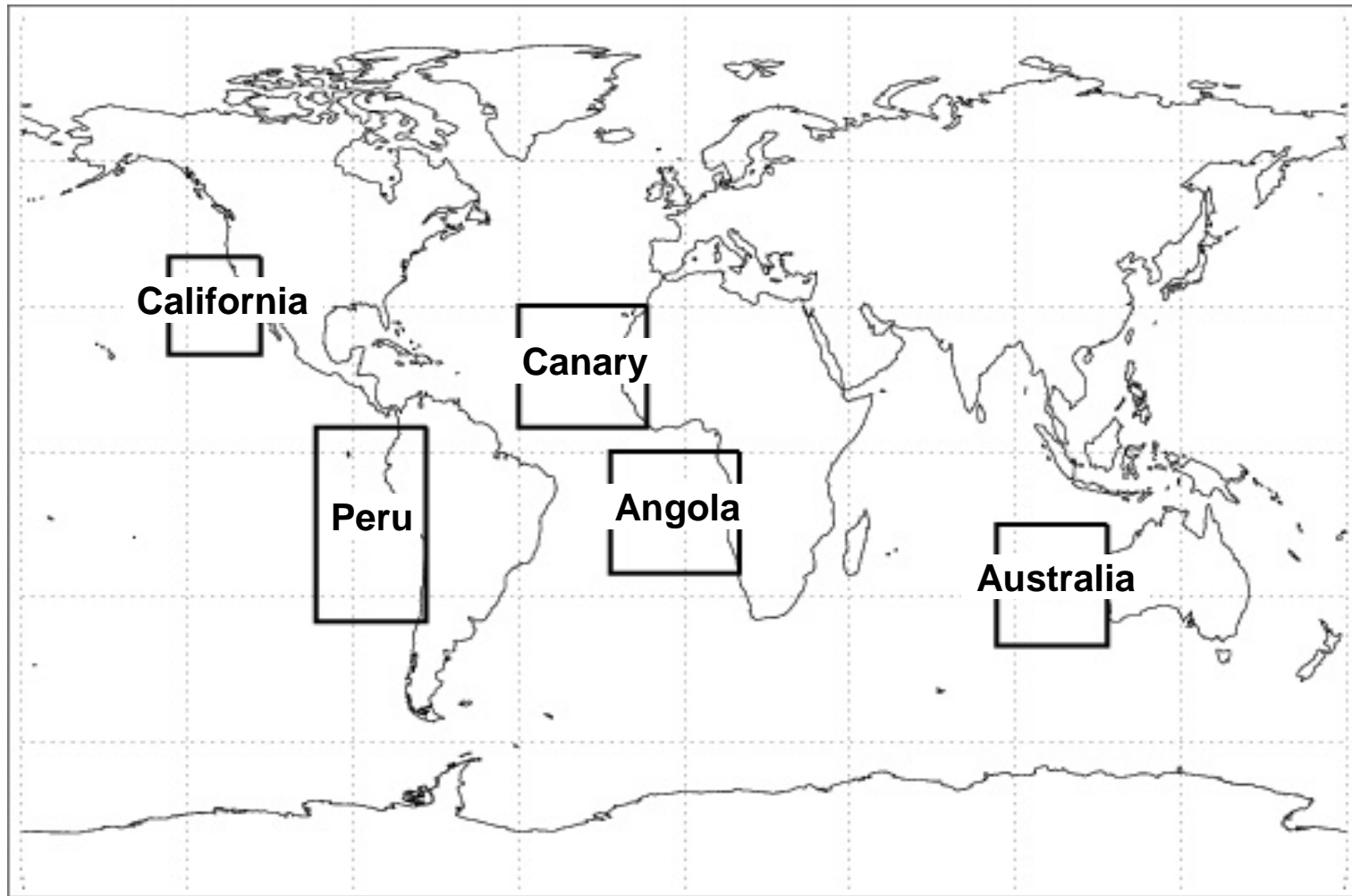


Figure 2. Map of marine boundary layer (MBL) cloud study regions. Each box indicates the location of a major MBL cloud region, based on the surface-based climatologies in Klein and Hartmann (1993) and Norris and Leovy (1994). The latitude-longitude bounds for each region are given in Table 1. Five-years of data are obtained for each study region, spanning March 2000 to February 2005. Cloud data over any land areas within the study regions are removed from the analyses.

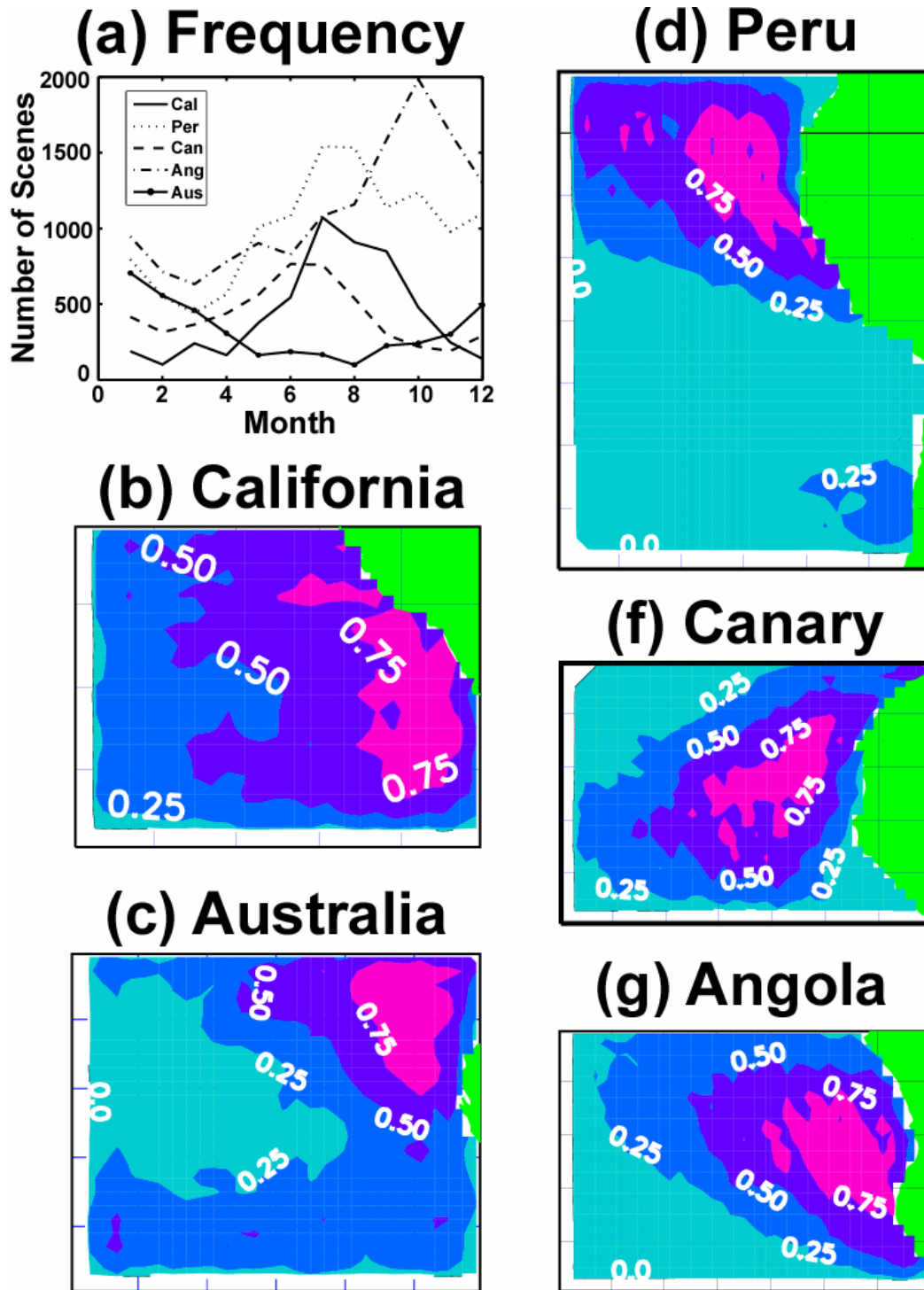


Figure 3. Occurrence frequencies of MBL cloud scenes. (a) Monthly frequencies per region. The numbers of MBL cloud scenes identified per month are combined from all years. (b – f) Regional variations in MBL cloud scene occurrence. For each region, the number of MBL scenes for all months are combined and gridded. Results are displayed as a fraction of the respective region’s maximum grid value (i.e., the maximum value in each 2-D plot is one). Occurrence frequency per region is binned on a 1° grid.

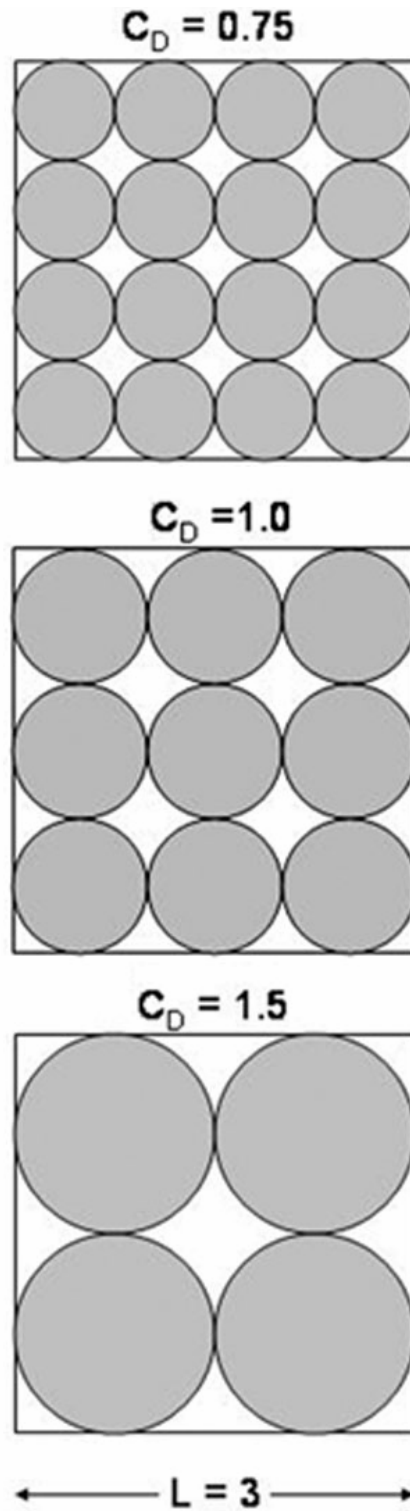


Figure 4. Idealized illustration of effective cloud diameter, C_D . For each scene composed of circular clouds, the cloud fraction is constant at 0.785, but C_D assumes a different value for each scene: 0.75, 1.0 and 1.5 (in arbitrary length units, L). This shows how C_D provides additional information to cloud fraction about how clouds are organized within a scene.

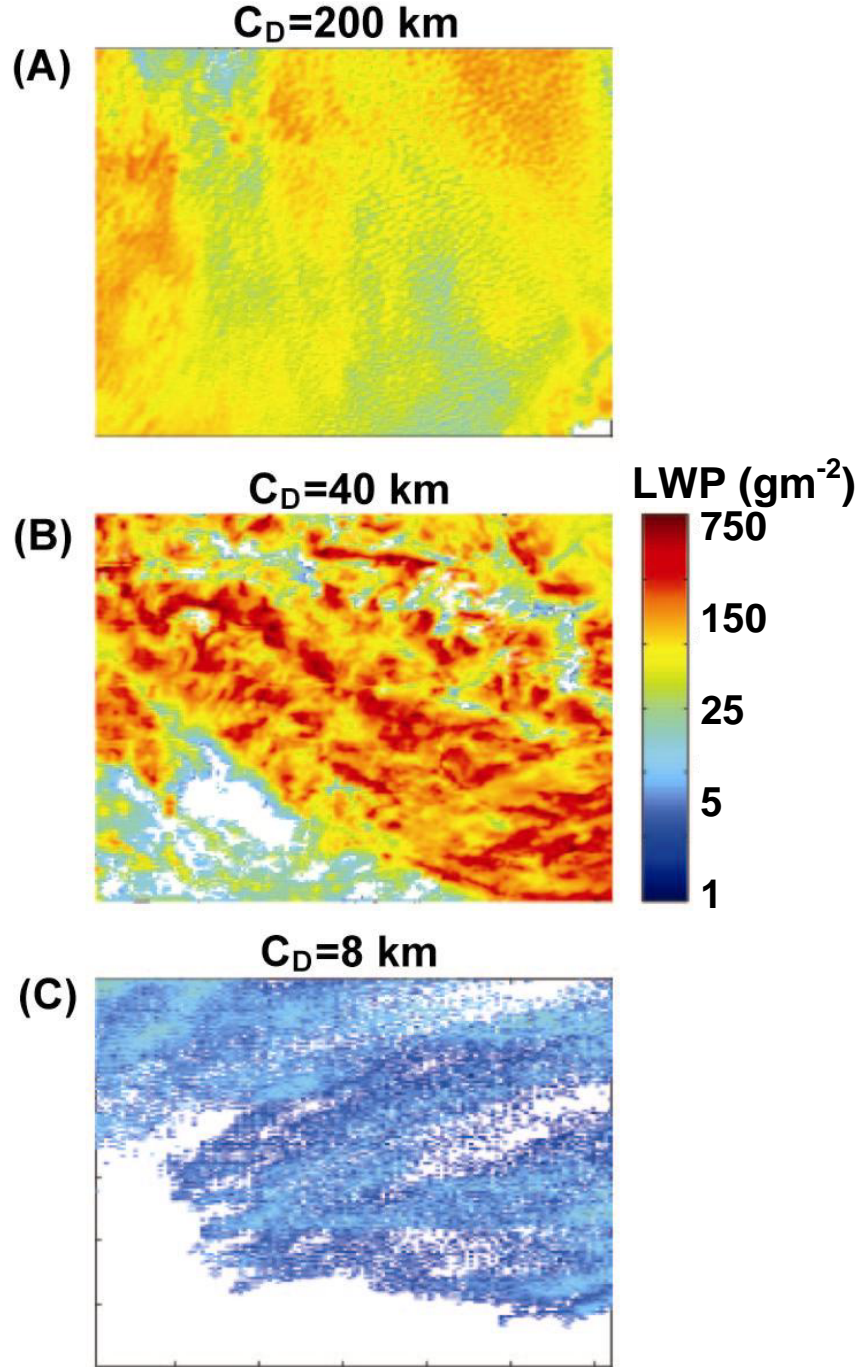


Figure 5. Marine stratus cloud structure and effective cloud diameter, C_D . The three MODIS scenes illustrate the appearance of the cloud LWP as C_D increases sequentially by a factor of five between each scene. Plotted are the \log_{10} of the LWP, where white is clear sky. For each scene, the effective cloud diameter (C_D), fractional cloud cover (f), mean cloud LWP (L) and standard deviation of the LWP (σ) are: A) $C_D=200$ km, $f=99\%$, $L=81 \text{ g m}^{-2}$, $\sigma=35 \text{ g m}^{-2}$; B) $C_D=40$ km, $f=83\%$, $L=189 \text{ g m}^{-2}$, $\sigma=132 \text{ g m}^{-2}$; C) $C_D=8$ km, $f=51\%$, $L=9.7 \text{ g m}^{-2}$, $\sigma=4.3 \text{ g m}^{-2}$.

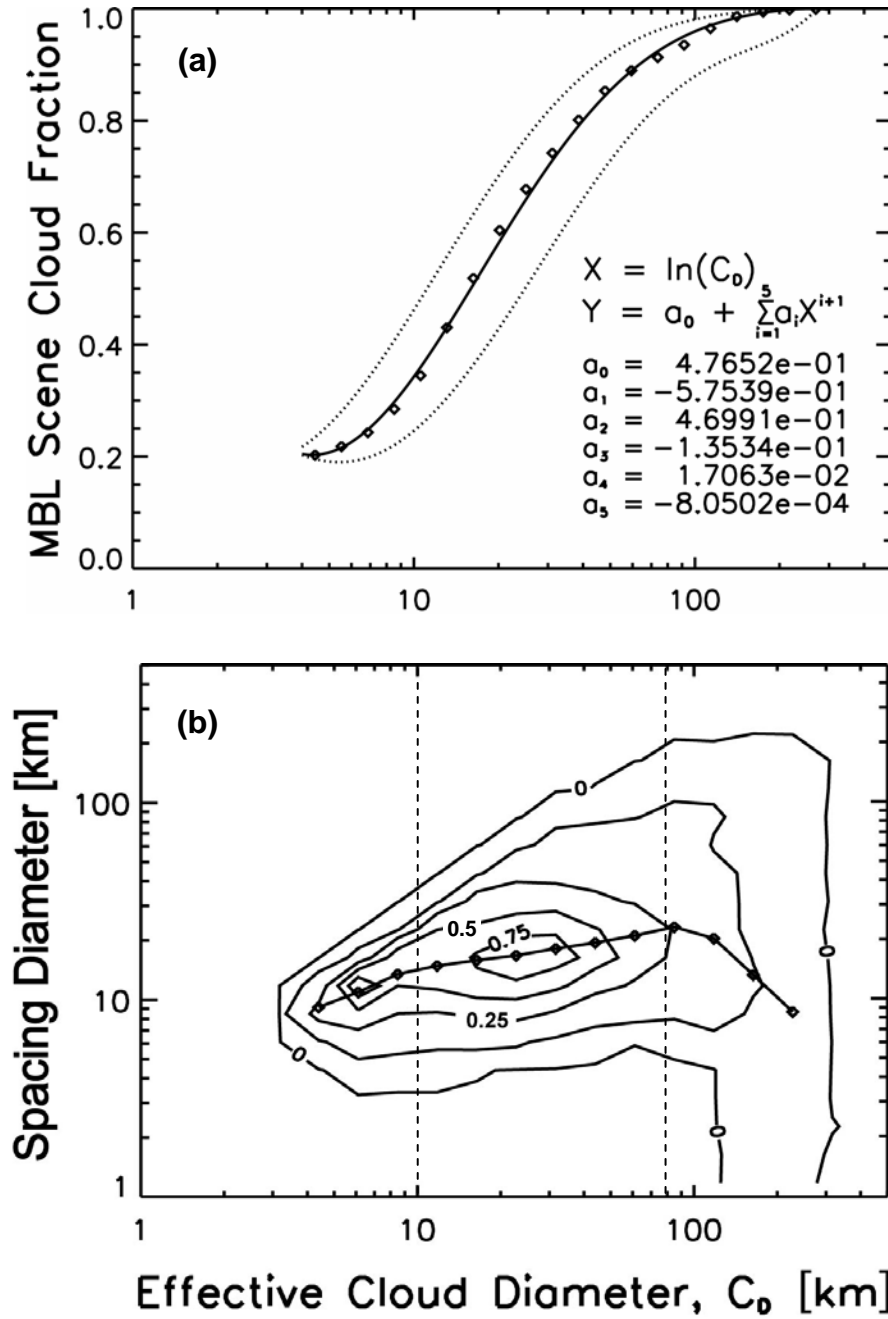


Figure 6. (a) MBL Cloud fraction and effective cloud diameter. The cloud fractions for all MBL cloud scenes are binned by $\ln(C_D)$ and the medians per bin are plotted (diamonds). A polynomial is fit to the median points (solid curve) and the coefficients provided. The polynomial is only applicable within the bounds of the data used for fitting, $4 \leq C_D \leq 300$ km. The scatter of the individual points about the median curve is indicated by the $\pm 25\%$ quartile levels per bin (dotted lines). (b) Cloud spacing and effective cloud diameter. The space between clouds is expressed as the diameter of an area-equivalent circle (see text for details). The counts per grid are normalized by the maximum grid value. Contours are 0.0, 0.05, 0.25, 0.50, and 0.75. Line with diamonds gives the median spacing diameters per $\ln(C_D)$ bin. The vertical dashed lines delineate groupings discussed in the text.

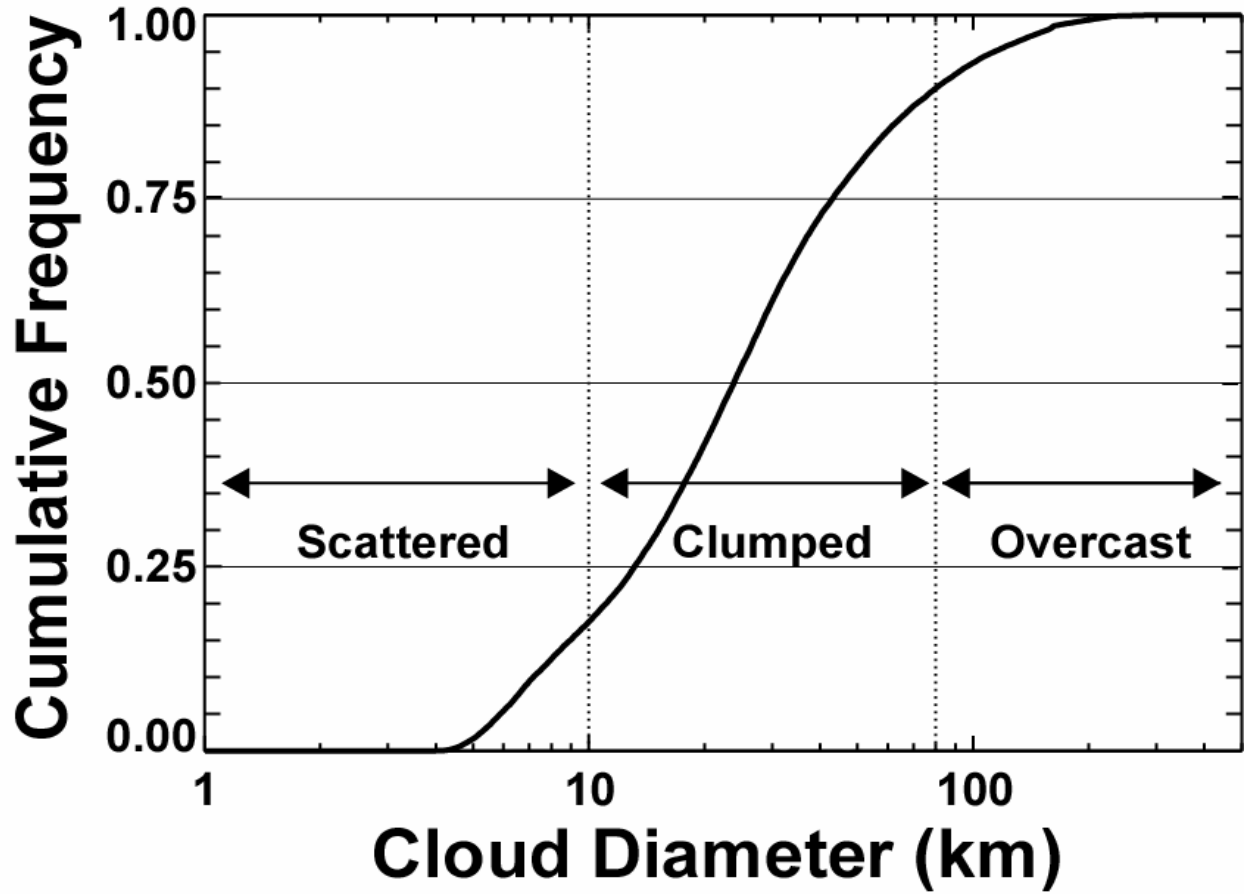


Figure 7. Cumulative frequency of occurrence of MBL effective cloud diameters, C_D . All regions and years combined in the plot. For ease of discussion, cloud scenes are divided into three descriptive categories: scattered, $C_D \leq 10$ km; clumped, $10 < C_D \leq 80$ km; and overcast, $C_D > 80$ km. The percentages of MBL scenes per category (scattered, clumped, and overcast) are approximately 20, 70, and 10%.

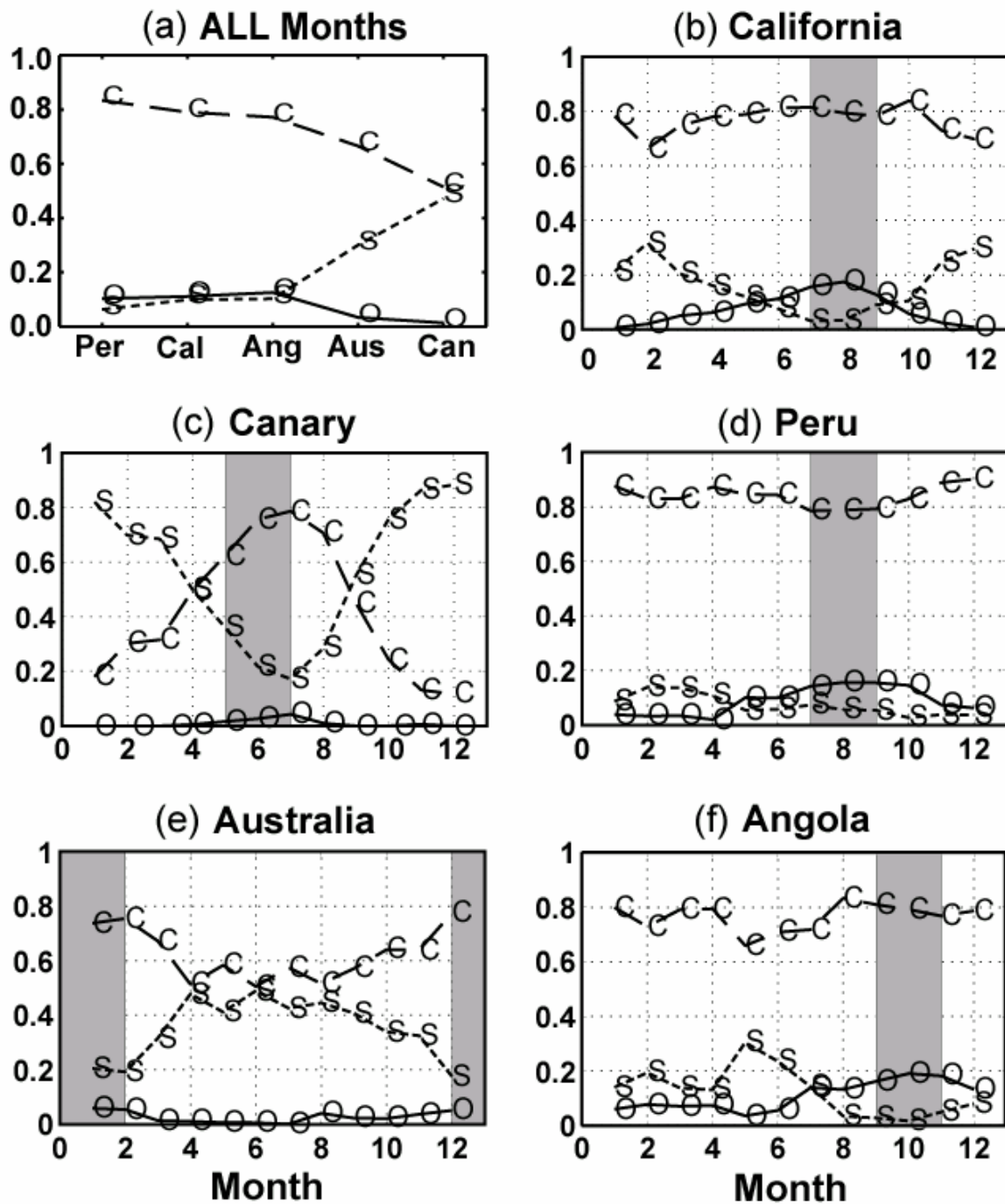


Figure 8. General MBL cloud structure per region. (a) All years and months are combined per region to show the total composition of each study region is given as a fraction of the three descriptive cloud categories: scattered (S), clumped (C), and overcast (O). (b-f) Seasonal cycle of MBL cloud structure per study region. The relative frequency of occurrence per month is given for each of the three cloud categories. Grey shading indicates the three months of peak MBL cloud occurrence per region.

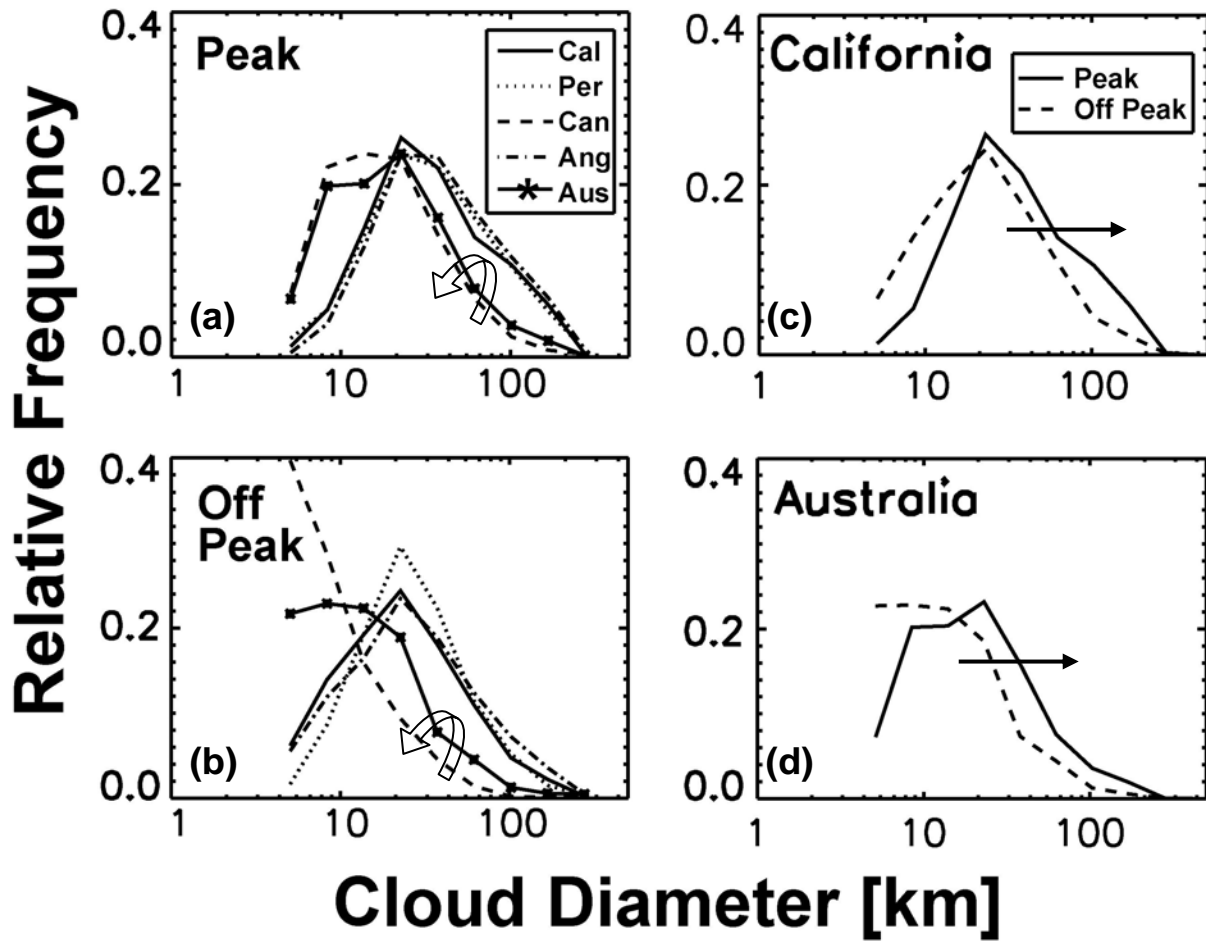


Figure 9. Relative frequencies of occurrence of C_D per region. (Left panels) All regions are placed on one plot partitioned by peak (top) and non-peak (bottom) months of MBL cloud occurrence. Semicircle groups Canary and Australia, which have similar distributions compared to the other three regions that share similar features (in vice versa). (Right panels) Results for the California (top) and Australia (bottom) regions, partitioned by the three peak (solid) and nine non-peak (dashed) months. A shift towards larger cloud diameters occurs during the peak months (including the regions not shown).

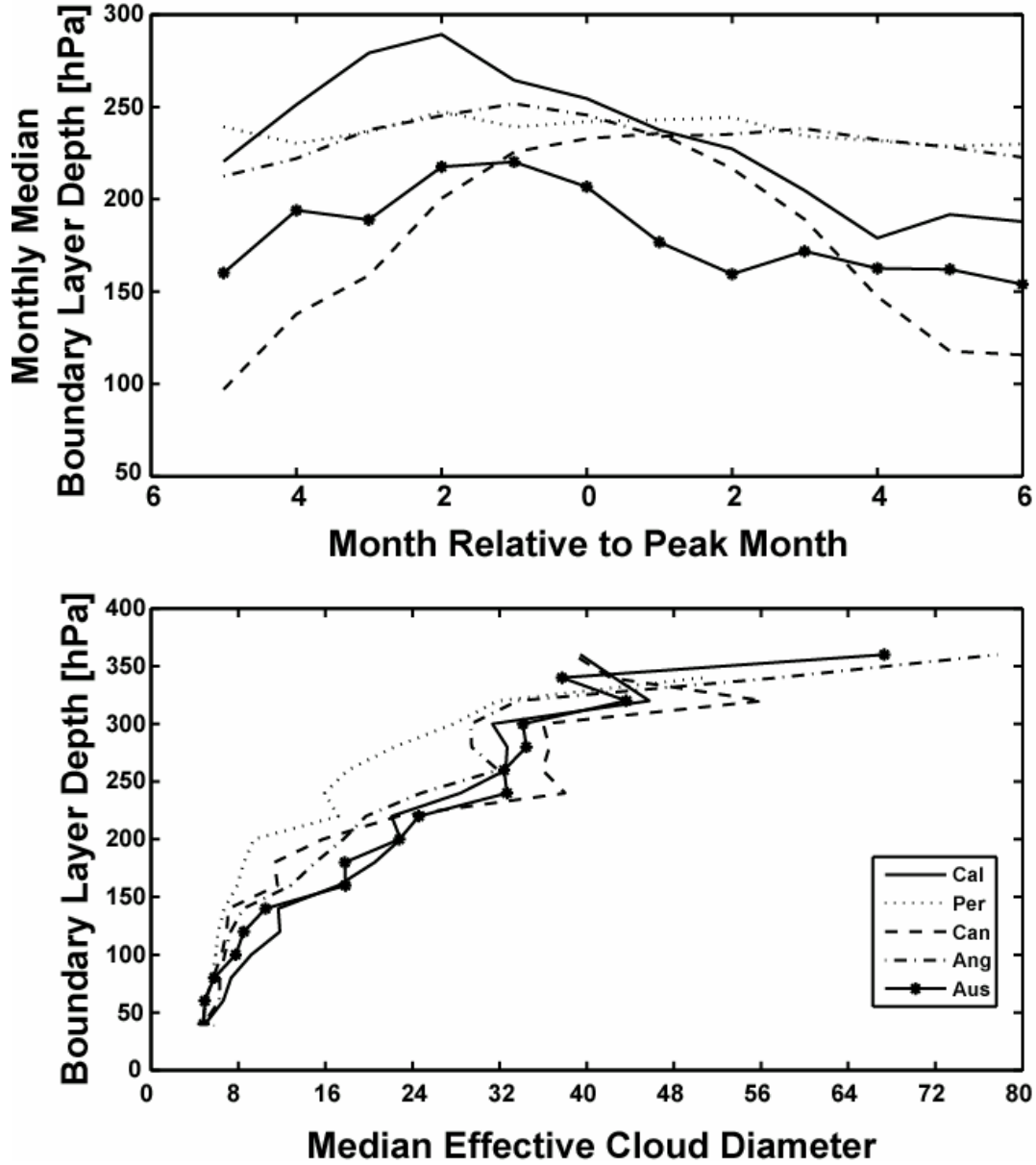


Figure 10. Boundary layer depth variation among regions. The legend in the bottom panel applies to all curves shown. (Top) Monthly variation in boundary layer depth per study region. Cloud-top pressure is used as a proxy for MBL depth, and its median value is determined per month per region. The abscissa is the month of year, given per region as an offset relative to the middle of its three peak months (i.e., zero is at the middle). The middle of the peak months per region are (from Table 1): Australia-January, Canary-June, California-August, Peru-August, Angola-October. (Bottom) Cloud-top pressure and C_D occurrence. C_D is binned by cloud-top pressures (20 hPa thick) and the median value per bin is plotted per region. All regions show an increase in median C_D with increasing boundary layer depth. The dynamic range in MBL height is larger in the lower panel than in the upper panel because it is binned by C_D and there is a positive correlation found between C_D and MBL height; conversely in the upper panel, the month-to-month dependence on C_D is weaker so the medians are derived from broad, monthly C_D distributions, which mutes the dynamic range of MBL height.

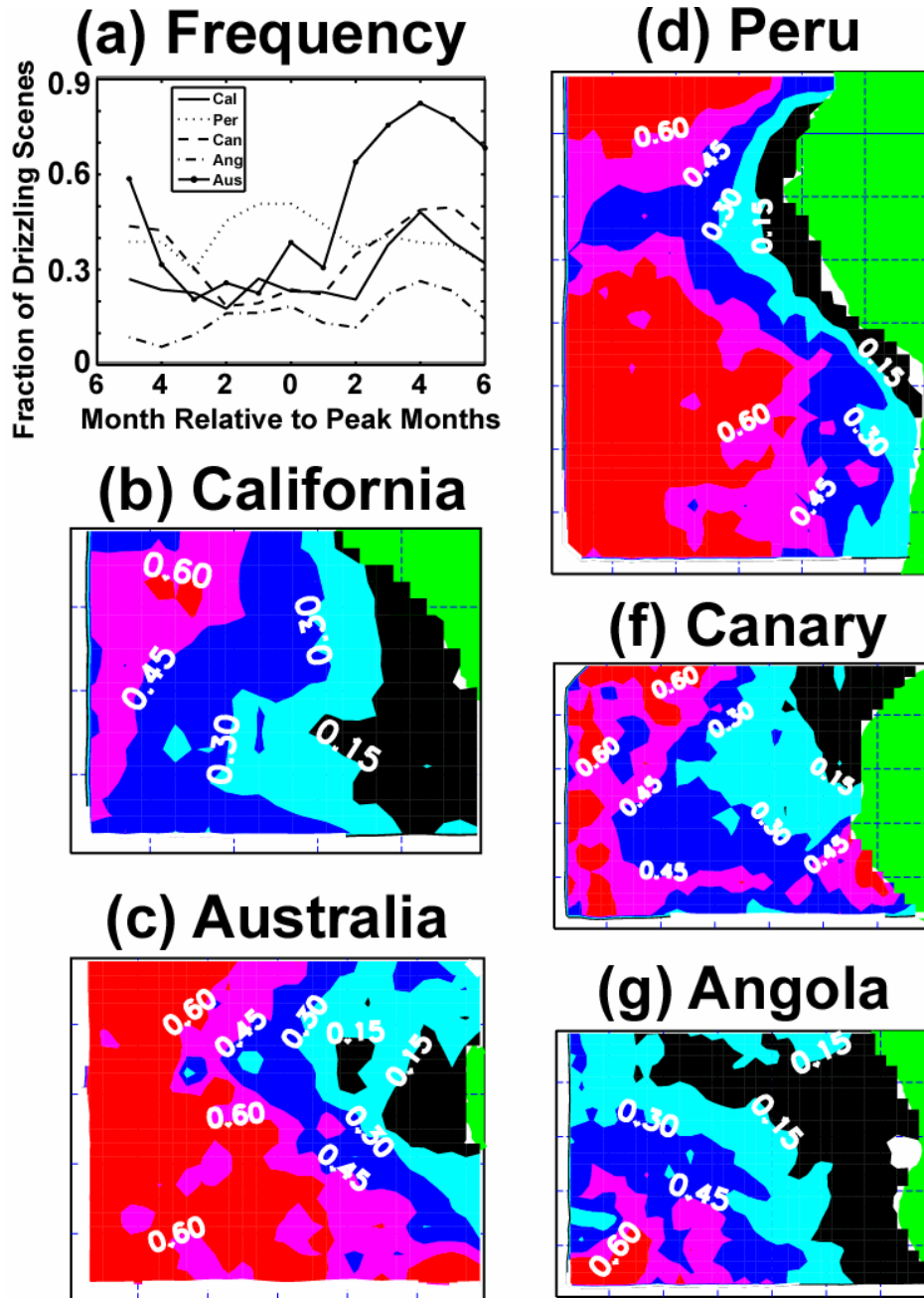


Figure 11. Geographical distribution of drizzle frequency. Drizzle scenes are defined as those with a mean $R_{\text{eff}} \geq 15 \mu\text{m}$ (Pinsky and Khain 2002; Masunaga et al. 2002; Shoa and Liu 2004). (a) Monthly variation of drizzle frequency. Plotted are the fractions of MBL scenes that meet the drizzle criterion per month. The abscissa is the month of year, given per region as an offset relative to the middle of its three peak months (explained in Figure 10). (b-f) Regional distribution of drizzling MBL cloud scenes. Shown are the fractions of MBL scenes that are drizzling per grid, where the scenes for all months are combined in a single grid per region. Contours of fractional occurrence are given for 0.15, 0.30, 0.45, and 0.60. Note that the total drizzle occurrence would be determined by weighting these fractions by the total frequency of MBL occurrence per grid. Occurrence frequency per region is binned on a 1° grid.

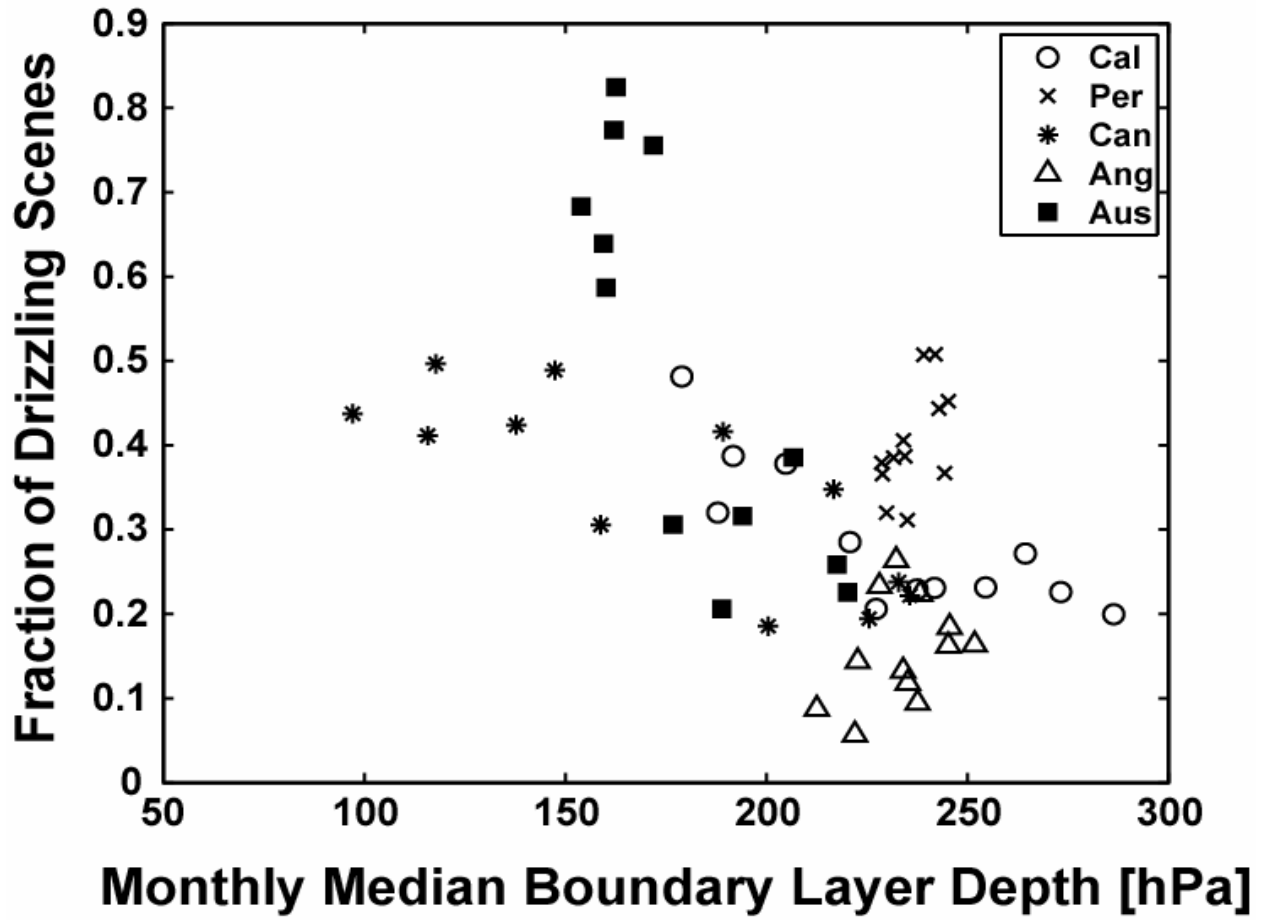


Figure 12. Boundary layer depth versus drizzle occurrence. The fractions of the total number of scenes per month that are drizzling are given as a function of the monthly median boundary layer depth (as defined in Figure 10a).

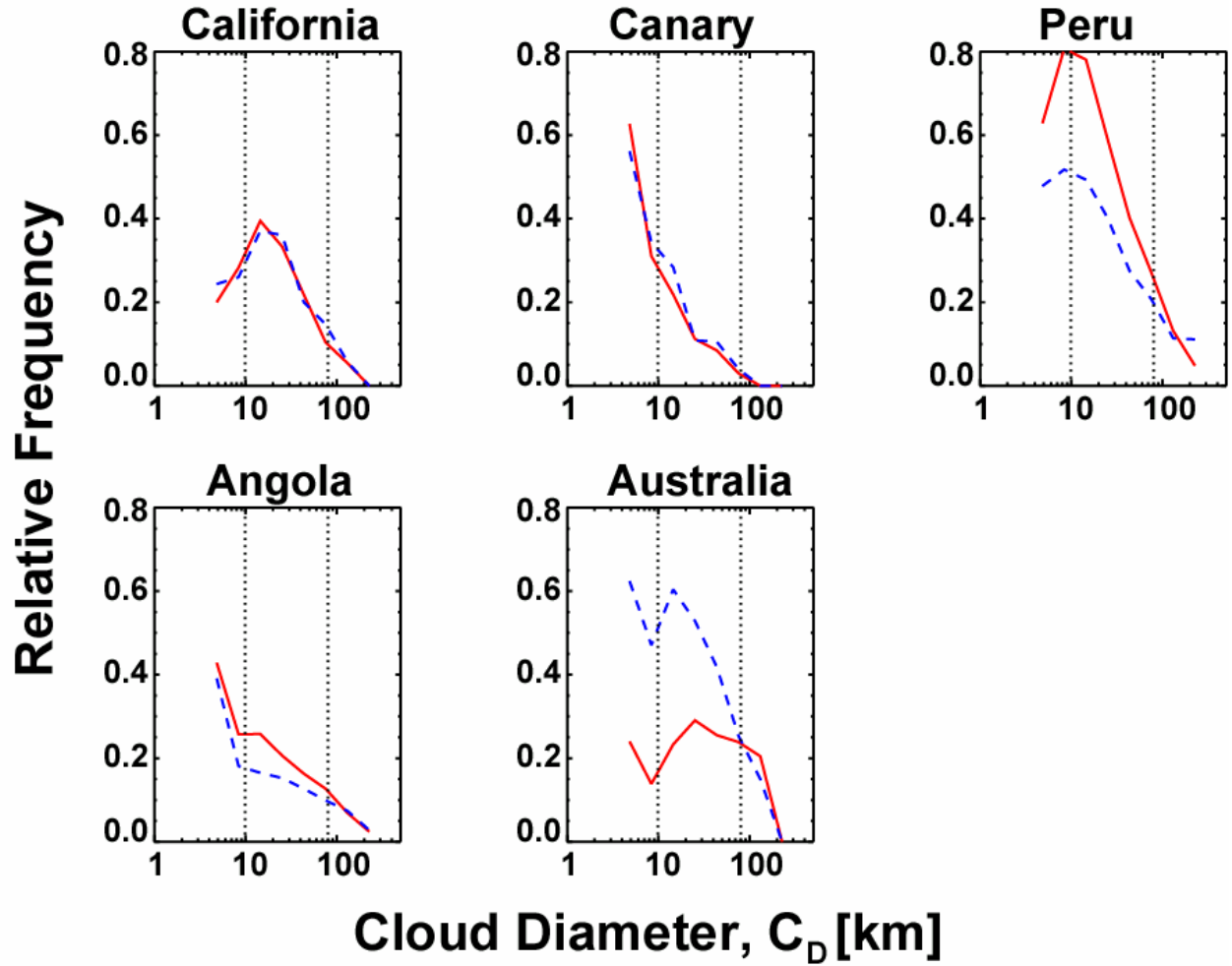


Figure 13. Frequency of drizzle occurrence as a function of effective cloud diameter, C_D . The drizzle frequencies are partitioned into two groups: the three months of peak MBL cloud occurrence within each region (red line), and the nine off-peak months (blue dashed line). Drizzle occurrence tends to be largest for the smaller values of C_D , which represent the more scattered cloud scenes. The frequencies for Canary and California show little sensitivity to peak versus off-peak timings, while Peru and Australia show pronounced differences in directions that are opposite from each other.

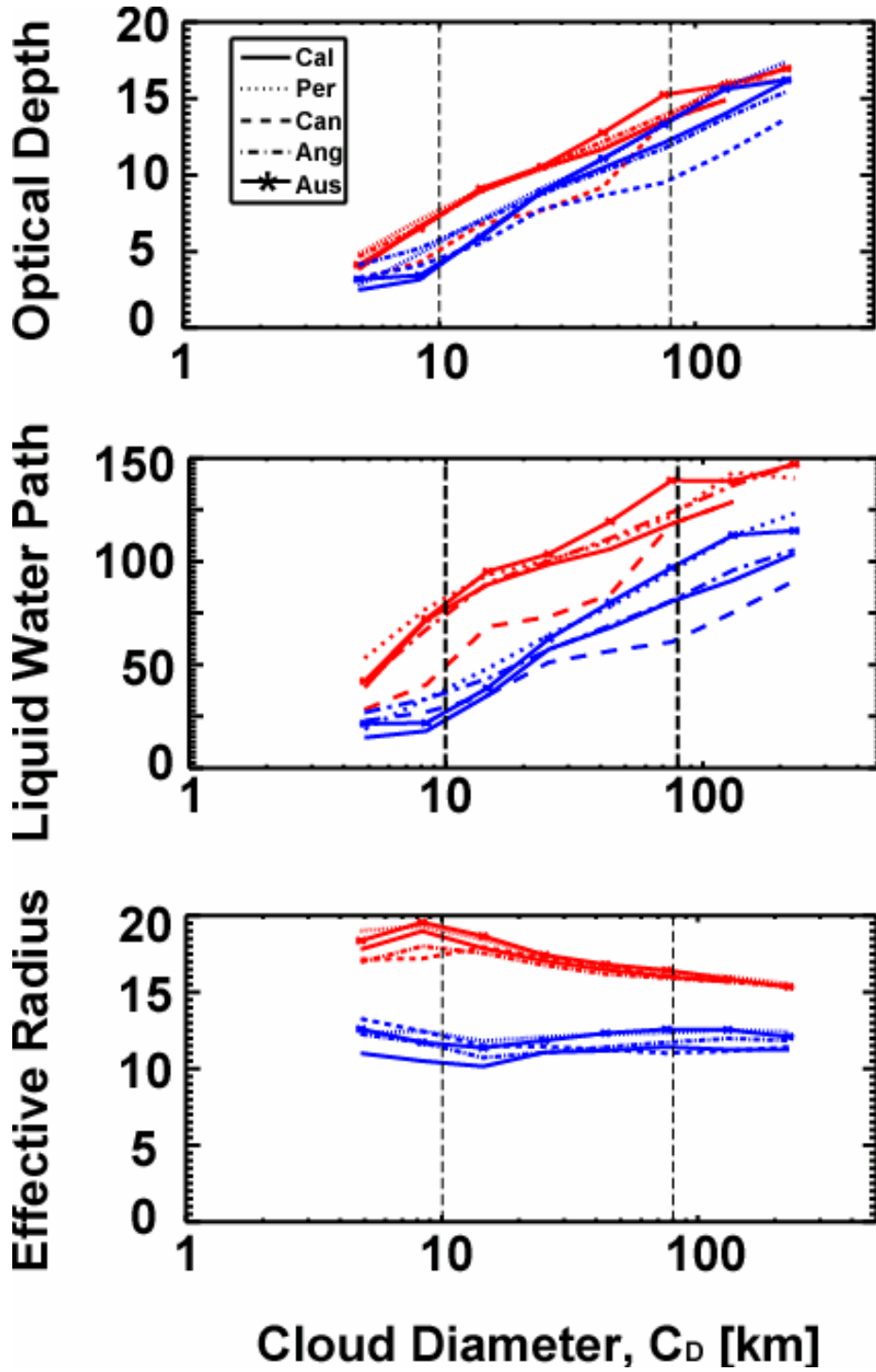


Figure 14. Dependence of MBL cloud properties on effective cloud diameter, C_D . MBL cloud optical depth, τ_{vis} (top), LWP (middle) and R_{eff} (bottom) are plotted as a function of the natural logarithm of C_D . For each curve, all data per region are separated into drizzling (red) and non-drizzling (blue) categories and binned using intervals that are $0.55C_D$ wide; the median for each bin is plotted.

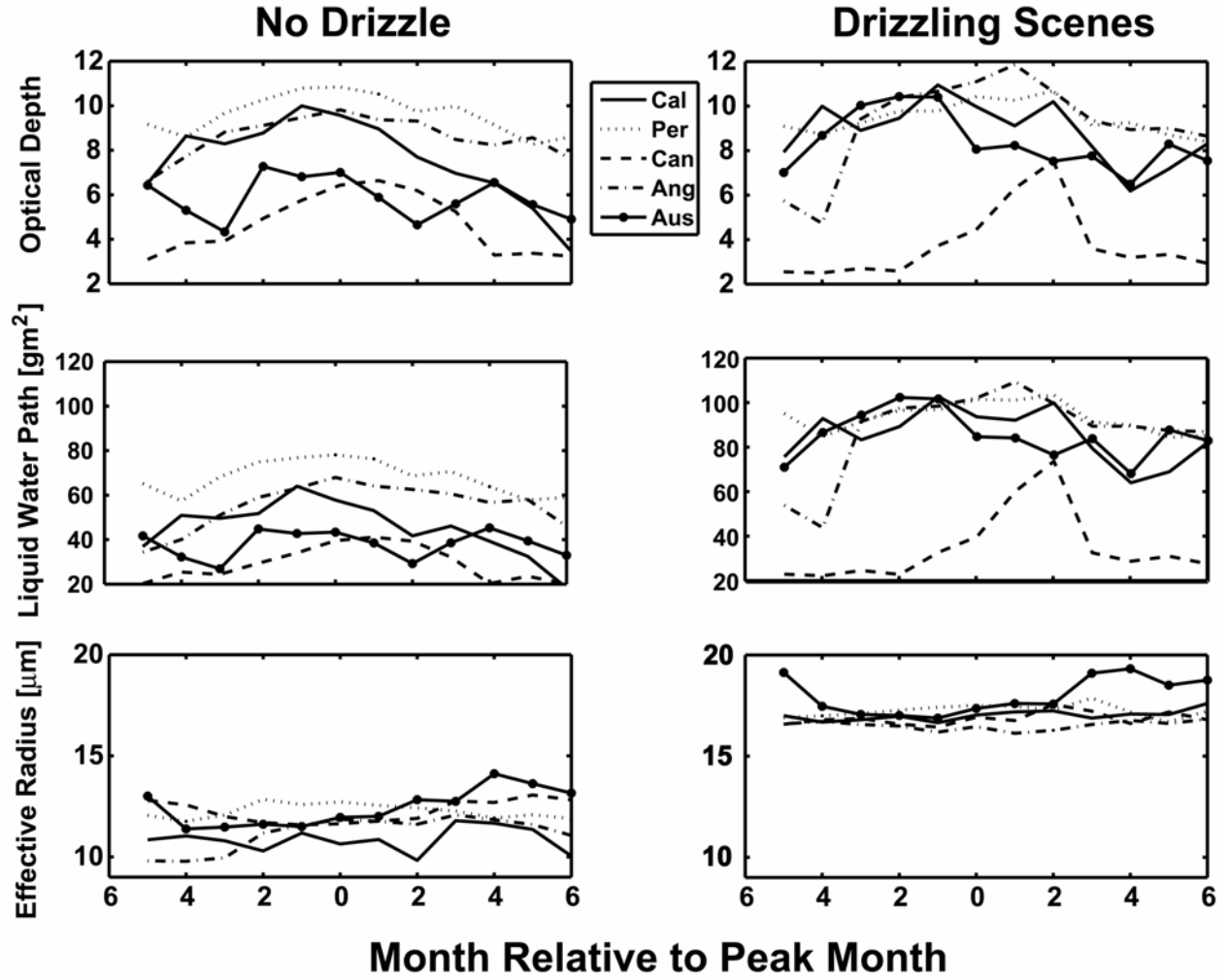


Figure 15. Monthly variation in MBL cloud properties. For each curve, all data per region are separated into drizzling and non-drizzling categories and their monthly means are plotted. Shown are the monthly means of MBL cloud optical depth, τ_{vis} (top), LWP (middle) and R_{eff} (bottom) for drizzling (right) and non-drizzling (left) scenes. The abscissa is the month of year, given per region as an offset relative to the middle of its three peak months (explained in Figure 10).